



Decoupling of zircon U–Pb and trace-element systematics driven by U diffusion in eclogite-facies zircon (Monviso meta-ophiolite, W. Alps)

Joshua M. Garber¹ · Andrew J. Smye¹ · Maureen D. Feineman¹ · Andrew R. C. Kylander-Clark² · Simon Matthews³

Received: 17 October 2019 / Accepted: 29 April 2020
© Springer-Verlag GmbH Germany, part of Springer Nature 2020

Abstract

Zircon is widely used to date metamorphic processes, particularly due to slow cation diffusion under crustal conditions. Here, we present laser-ablation depth profiling data that demonstrate rapid U diffusion in partially altered, high-pressure zircon. The zircons are hosted in metagabbros that underwent eclogite-facies (~550 °C, ~2.6 GPa) recrystallization during subduction of the Monviso meta-ophiolite. One metagabbro contains only newly grown zircons (50.2 ± 1.1 Ma); two coarser-grained samples exhibit thin metamorphic rims on igneous cores. Most profiles in the coarse-grained samples record discrete Pb_C-rich and Pb^{*}-, U-, Th-, and trace-element poor rims in the outermost ≤ 5 μm of each grain, but U shows apparent diffusion profiles that extend ~10–15 μm into zircon crystals and correlate with U–Pb date resetting. The data define three populations (cores, diffusively reset rims, and newly precipitated rims) that form two two-component mixtures, indicating that recrystallization was everywhere coupled with U addition. Data from fully equilibrated rims form a single age population (51.1 ± 0.4 Ma) within error of the newly grown zircon and compatible with ~1 My fluid–rock interaction timescales. We interpret the U profiles as evidence of inward U diffusion associated with fluid-induced resorption, and systematically exclude other mechanisms for their formation. However, calculated diffusivity estimates are >20 orders of magnitude faster than predicted by experiments. The absence of zircon lattice damage, and the propagation of diffusion inward of a reaction front, indicates a link between fluid-saturated zircon alteration and fast U diffusion in zircon. Our results emphasize that—even at low temperature—zircon U–Pb systematics may be affected by parent and/or daughter diffusion over length scales large enough to affect laser-ablation or ion microprobe spot analyses.

Keywords Zircon · U–pb geochronology · Trace elements · Recrystallization · Dissolution-reprecipitation · Diffusion

Introduction

Zircon (ZrSiO_4) provides an unparalleled record of metamorphic processes (Rubatto 2017). It often preserves multiple stages of growth, recrystallization, and/or radiation damage (e.g., Rubatto et al. 2011; Pidgeon 2014; Gauthiez-Putallaz et al. 2016); it may undergo growth, recrystallization, or alteration at all stages along the metamorphic path from diagenesis to anatexis (e.g., Vavra et al. 1999; Spandler et al. 2004; Harley et al. 2007; Rubatto 2017); it is a sensitive recorder of fluid- and melt-rock reactions (e.g., Tomaschek et al. 2003; Geisler et al. 2007; Soman et al. 2010); and as the principal sink for Zr in metamorphic rocks (e.g., Rubatto and Hermann 2003), it crystallizes in a wide range of bulk compositions (Belousova et al. 2002). Zircon is particularly useful because of slow rates of thermally activated volume diffusion of Pb, U, Th, rare-earth elements (REE), Hf, and O under most crustal metamorphic conditions (Cherniak et al.

Communicated by Daniela Rubatto.

Electronic supplementary material The online version of this article (<https://doi.org/10.1007/s00410-020-01692-2>) contains supplementary material, which is available to authorized users.

✉ Joshua M. Garber
jmgarber@psu.edu

¹ Department of Geosciences, The Pennsylvania State University, University Park, PA, USA

² Department of Earth Science, University of California, Santa Barbara, CA, USA

³ Department of Earth and Planetary Sciences, Johns Hopkins University, Baltimore, MD, USA

1991; Cherniak et al. 1997a, b; Lee et al. 1997; Watson and Cherniak 1997; Cherniak and Watson 2001). This nominally prevents disturbances to zircon U–Pb–Hf–O isotopes and trace elements once recrystallization or growth has ceased, and makes zircon a faithful recorder of metamorphic reactions (e.g., Gauthiez–Putallaz et al. 2016), even in ultrahigh-temperature metamorphic rocks (e.g., Taylor et al. 2017).

However, there have been many reported cases of isotope and trace-element decoupling in zircon over a wide range of metamorphic conditions. Several of these examples result from low- T (< 200 °C) saline fluid interaction with metamict zircon ("diffusion–reaction": Geisler et al. 2002, 2003a, b), in which partial to complete U–Pb date resetting due to diffusive U or Pb gain or loss is correlated with the diffusion of non-stoichiometric components (e.g., Ca, Al) into damaged or amorphous zircon (cf. Geisler et al. 2007; Seydoux-Guillaume et al. 2015). Another common recrystallization mechanism involves dissolution–reprecipitation, in which trace-element-rich zircon domains dissolve in a fluid or melt, and a new trace-element-poor zircon is precipitated (Pidgeon 1992; Tomaschek et al. 2003; Putnis et al. 2005; Geisler et al. 2007; Putnis 2009; Soman et al. 2010). Such alteration rims are often clearly identified in cathodoluminescence (CL) images (Rubatto and Gebauer 2000) and may exhibit incompletely to fully reset U–Pb dates, ϵ_{Hf} , $\delta^{18}\text{O}$, and trace elements, along with micropores, low zircon Th/U (≤ 0.1), and exsolved Th- and U-rich phases (Tomaschek et al. 2003; Martin et al. 2008; Chen et al. 2010; Soman et al. 2010; Rioux et al. 2015; Štípská et al. 2016). Micro- to nanoscale investigations of zircon demonstrate that Pb mobility is the principal driver for zircon age perturbations and that its behavior is not necessarily correlated with that of other elements. Examples include the migration of Pb without U and Th mobility, leading to reverse discordance (Wiedenbeck 1995; Kusiak et al. 2013), and the sequestration of zircon Pb in partial-melt related nanospheres (Kusiak et al. 2015), dislocation loops (Peterman et al. 2016), and compositionally distinct clusters (Valley et al. 2014).

Understanding the mechanisms by which zircon isotope and trace-element systematics are altered during metamorphism is important for relating U–Pb dates to petrogenesis (Rubatto 2017). In addition to Rutherford backscattering (RBS, e.g., Cherniak et al. 1997a) and secondary-ion mass spectrometry (SIMS) depth-profiling techniques (e.g., Grove and Harrison 1999), laser-ablation (LA) single-shot and depth-profiling inductively coupled plasma mass spectrometry (ICPMS) methods (Cottle et al. 2009, 2012; Smye and Stockli 2014; Steely et al. 2014; Viete et al. 2015; Stearns et al. 2016; Lima et al. 2018; Rasmussen et al. 2019) have the potential to address these questions by facilitating analytical length scales intermediate between < 100 nm atom-probe tomography (APT) or transmission electron microscope (TEM) techniques and 15–30 μm sensitive

high-resolution ion microprobe (SHRIMP) or LA-ICPMS spot analyses. Such length scales help relate the effects of nanoscale compositional textures to microscale isotopic measurements (cf. Valley et al. 2014).

With the intent of constraining timescales of eclogite-facies metamorphism, and understanding zircon U–Pb and trace-element systematics during deep subduction, we performed laser-ablation split-stream (LASS: Kylander-Clark et al. 2013) continuous depth profiling on metamorphic zircon rims from Fe–Ti metagabbros in the Monviso metaophiolite—an archetypal example of exhumed high-pressure (HP) oceanic crust. The data are augmented by observations from cathodoluminescence (CL) images, Raman spectroscopy, and nanoscale field-emission scanning electron microscopy (FE-SEM). Zircons from similar rocks at the same locality have been previously subjected to SHRIMP U–Pb, trace-element, and oxygen isotope measurements (Rubatto and Hermann 2003; Rubatto and Angiboust 2015), providing essential context for our work. Our dataset is consistent with previous interpretations suggesting fluid-driven partial recrystallization over ≤ 1 My (Rubatto and Angiboust 2015; Broadwell et al. 2019), but U–Pb age resetting occurs much further into each crystal than expected from the width of recrystallized rims. We attribute these data to elevated U (and potentially Pb) mobility in zircon, and discuss discrepancies between our observations and experimentally measured data.

Geologic background and sample description

The zircons analyzed herein are from metagabbros in the Monviso metaophiolite, Western Alps (Fig. 1). Rocks in the Western Alps record the closure of a hyperextended rift margin (Lagabriele and Lemoine 1997; Lagabriele et al. 2015), involving the subduction and collision of the European Plate beneath Africa (Coward and Dietrich 1989; Beltrando et al. 2010). The Monviso metaophiolite is part of a ~ 300 km belt of blueschist- to eclogite-facies ophiolitic material detached from the downgoing oceanic slab, representing sedimentary, mafic, and ultramafic remnants of the subducted Ligurian–Piemontese Ocean (Lagabriele and Cannat 1990; Lagabriele and Lemoine 1997; Agard et al. 2001, 2009; Angiboust et al. 2009; Vitale Brovarone et al. 2011; Lagabriele et al. 2015). The ophiolite consists of two relatively coherent thrust sheets juxtaposed during exhumation: the overturned, upper Monviso Unit (MU) is composed of Mg–Al metagabbros, pillow basalts, and sediments, with the upright Lago Superiore Unit (LSU) consisting of serpentinized peridotites, Mg–Al and Fe–Ti gabbros, pillow basalts, and sediments (Lombardo et al. 1978; Angiboust et al. 2012b). Peak pressure–temperature (P – T)

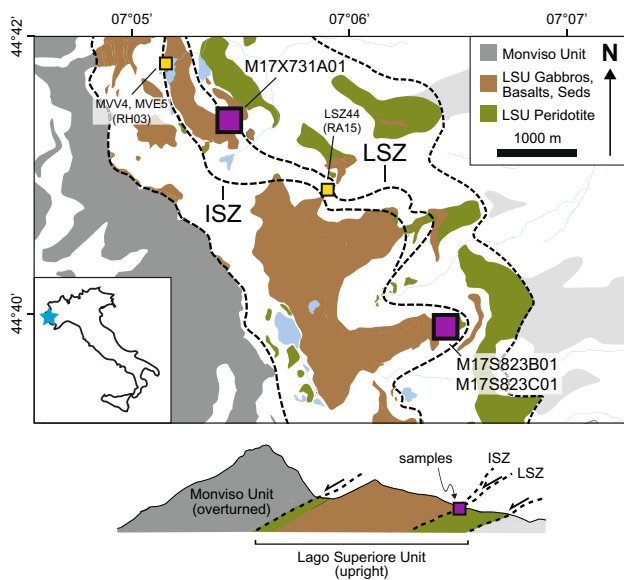


Fig. 1 Lithologic map and schematic cross-section of the Monviso meta-ophiolite, modified from Angiboust et al. (2012b). Dashed black lines indicate major ductile shear zones that separate the overlying, lower- T Monviso Unit from the higher- T Lago Superiore Unit (LSU). Samples from this study (purple squares) are taken from Fe-Ti gabbro outcrops within or above shear zones along the gabbro-serpentinite contact of the ophiolite, in a similar structural position to those from previous studies (yellow squares). *LSZ* Lower Shear Zone, *ISZ* Intermediate Shear Zone, RH03 = Rubatto and Hermann (2003), RA15 = Rubatto and Angiboust (2015)

conditions determined by pseudosection and conventional thermobarometric techniques are consistent within each unit (Angiboust et al. 2012b), with the LSU reaching ~ 26 kbar, ~ 550 °C and the MU achieving ~ 22 kbar, ~ 480 °C (Groppo and Castelli 2010; Angiboust et al. 2012b; Locatelli et al. 2018). A prograde path calculated from P - T and T - fO_2 pseudosection modelling of a lawsonite eclogite in the LSU documents a significant pressure increase (from ~ 17 to 25 kbar) and reduction in oxygen fugacity over a narrow T interval (from ~ 450 to 550 °C) (Groppo and Castelli 2010).

The LSU is transected by ductile shear zones that were active at peak, eclogite-facies conditions (Angiboust et al. 2011, 2012b) and were accompanied by significant metasomatism, mass transfer, veining, and brecciation (Philippot and Kienast 1989; Philippot and Selverstone 1991; Spandler et al. 2011; Angiboust et al. 2014; Locatelli et al. 2018). Whereas the structurally higher Intermediate Shear Zone (ISZ; Fig. 1) records only locally derived fluids without brecciation (Angiboust et al. 2011, and references therein), the Lower Shear Zone (LSZ; Fig. 1)—separating gabbros and serpentinized peridotites—exhibits several cycles of eclogite-facies veining, brecciation, cementation, and fluid infiltration (Angiboust et al. 2012a; Locatelli et al. 2018; Broadwell et al. 2019). Trace-element and isotopic analyses of LSZ veins and eclogites implicate both locally sourced

and external, serpentinite- and sediment-derived fluids (Philippot and Kienast 1989; Philippot and Selverstone 1991; Spandler et al. 2011; Angiboust et al. 2014; Rubatto and Angiboust 2015; Locatelli et al. 2018).

Previous zircon geochronology at Monviso has focused on the timing of fluid flux and shear zone activity. Synchronous SHRIMP dates from newly grown zircons from an eclogite-facies omphacite-garnet vein in the ISZ (45 ± 1 Ma) (Rubatto and Hermann 2003) and recrystallized zircons from a metasomatized gabbro block rind (45.8 ± 0.7 Ma) (Rubatto and Angiboust 2015) document short fluid-rock interaction timescales that were apparently synchronous across the ophiolite (further supported by major-element diffusion speedometry on fractured garnets: Broadwell et al. 2019). In some cases these zircons show partial U-Pb date resetting of igneous cores (163 ± 2 Ma: Rubatto and Hermann 2003) that retain inherited oxygen isotope compositions, whereas fully reset metamorphic rims (45 ± 1 Ma) have uniformly lower $\delta^{18}O$ (Rubatto and Angiboust 2015). Several other studies have dated similar Fe-Ti gabbros from Monviso, yielding 62 ± 9 and 60 ± 12 Ma garnet-omphacite Sm-Nd isochron ages and 41.6 ± 0.4 and 39.2 ± 0.8 Ma phengite-omphacite Rb-Sr isochron ages (Cliff et al. 1998), a 49.1 ± 1.2 Ma garnet-whole-rock Lu-Hf isochron age (Duchêne et al. 1997), and Ar/Ar phengite dates that span ~ 53 –47 Ma (Monié and Philippot 1989).

Samples analyzed in this study are pervasively transformed Fe-Ti-rich gabbros (cf. Philippot and Kienast 1989; Angiboust et al. 2012b) located within or adjacent to the LSZ (Fig. 1). Sample M17X731A01 (henceforth referred to as A01; $44.68888^\circ N$, $7.09804^\circ E$; IGSN: EXT00001N) is a fine-grained (average garnet grain size ~ 200 μm), compositionally banded grt-omph-chl-rt-ap (abbreviations after Whitney and Evans 2010) metagabbro collected from within the LSZ in the vicinity of Lago Superiore (Fig. 1). The rock also contains rare monazite and epidote-rimmed allanite. Zircon occurs as equant, prismatic grains included within both matrix and porphyroblast phases, with a maximum diameter of ~ 80 μm . Samples M17S823B01 (B01; $44.66513^\circ N$, $7.12946^\circ E$; IGSN: EXT0000DR) and M17S823C01 (C01; $44.66473^\circ N$, $7.12995^\circ E$; IGSN: EXT0000DS) were taken from coarser-grained, folded, and banded eclogite blocks near Rifugio Alpetto (Fig. 1). These samples are from a structurally higher position than sample A01, in contact with more primitive Mg-Al gabbros in the uppermost part of the LSZ. Sample B01 contains peak assemblages dominated by garnet, omphacite, and rutile, with abundant ep-pg-chl-cpx-qtz pseudomorphs after lawsonite (locally ≤ 2 mm in size) and rare talc, apatite, phengite, and sulfides. Sample C01 is texturally and mineralogically similar to B01 but phengite, talc, and former lawsonite are less abundant, clinozoisite occurs as isolated matrix grains, and the sample is crosscut by an albite + chlorite, greenschist-facies vein. Zircons in

these two samples are elongate (aspect ratios of 2 or 3:1), prismatic, but partially pitted and corroded. They occur as inclusions in all major rock-forming phases, with maximum diameters < 200 μm .

All samples in this study contain textural and compositional features typical for eclogite-facies Monviso metagabbros, including compositional banding defined by variations in the modal abundance of major phases (primarily garnet and omphacite), atoll garnets (rare in B01 and common in C01 and A01), fractured/fluid-altered garnet chemical zoning, and two coexisting omphacites (e.g., Lombardo et al. 1978; Angiboust et al. 2012a, b)—suggesting that these samples followed a P – T – t evolution similar to rocks previously described in the literature. However, though such gabbros are often identified as mylonitic (Angiboust et al. 2012b), elongate grains of all metamorphic phases are randomly oriented across each thin section, and the only evident foliation is compositional. Any ductile strain was, therefore, accommodated before the final episode of mineral growth or recrystallization in these samples.

Analytical methods

Laser-ablation split stream (LASS) depth-profiling

Rock samples were disaggregated using high-voltage pulses with a SELFRAG fragmentation system at the Goethe University, Frankfurt; separates were washed, panned, magnetically separated using a Frantz Isodynamic Separator, and picked in ethanol using a binocular microscope at Penn State. Zircon whole grains and fragments from each sample were mounted in epoxy with unpolished crystal facets exposed.

LASS depth-profiling was performed at the University of California, Santa Barbara. U–Pb isotopes and trace-element data were collected simultaneously on the same spot (Kylander-Clark et al. 2013). Samples were ablated using a Photon Machines 193 nm excimer laser with a HelEx ablation cell coupled to a Nu Instruments Plasma 3D multicollector inductively-coupled plasma mass spectrometer (MC-ICPMS) for U–Pb measurements, and an Agilent 7700X quadrupole ICPMS for trace-element analyses. ^{238}U and ^{232}Th were detected on Faraday cups whereas ^{202}Hg , ^{204}Pb , ^{206}Pb , ^{207}Pb , and ^{208}Pb were collected on Daly detectors. Samples were run during the same session. Smaller ($\leq 80 \mu\text{m}$) zircons from M17X731A01 were analyzed with a 25- μm spot size, whereas larger zircons from M17S823B01 and M17S823C01 were run with a 50 μm spot size. The laser fluence at the sample surface was identical for all experiments at $\sim 1.5 \text{ J/cm}^2$. The laser was first fired twice with a 25–50 μm spot to remove surface contamination and this material was allowed to wash out for 15 s. Material was

then continuously ablated for 150 shots (M17X731A01) or 300 shots (M17S823B01 and C01) at a 2 Hz repetition rate, yielding total ablation times of 75 and 150 s, respectively. Pit morphologies and depths were characterized on a Nexview Zygo 3D Optical Profilometer at the Materials Characterization Lab at Penn State. All pits have steep, near-vertical walls and flat bottoms, with depths $\sim 8 \mu\text{m}$ (M17X731A01) and $\sim 15 \mu\text{m}$ (M17S823B01 and C01), yielding an ablation depth per shot of $\sim 50 \text{ nm}$. Analyses of unknowns were bracketed by analyses of matrix-matched zircon reference material (RM) 91500 ($1062.4 \pm 0.4 \text{ ID-TIMS } ^{206}\text{Pb}/^{238}\text{U}$ date: Wiedenbeck et al. (1995)), which was used as the primary RM for U–Pb isotopic analyses. Zircon RMs GJ-1 [$601.7 \pm 1.3 \text{ ID-TIMS } ^{206}\text{Pb}/^{238}\text{U}$ date: Jackson et al. (2004); Kylander-Clark et al. (2013)], Plešovice ($337.13 \pm 0.37 \text{ ID-TIMS } ^{206}\text{Pb}/^{238}\text{U}$ date: Sláma et al. (2008)), and Piexé [$564 \pm 4 \text{ Ma ID-TIMS } ^{206}\text{Pb}/^{238}\text{U}$ date: Dickinson and Gehrels (2003)] were used as secondary standards, with GJ-1 further serving as the primary trace-element RM. Using the same parameters and methods applied to unknowns, we obtained $^{207}\text{Pb}/^{206}\text{Pb}$ -corrected $^{206}\text{Pb}/^{238}\text{U}$ concordia dates of $602.8 \pm 1.0 \text{ Ma}$ for GJ-1, $335.9 \pm 1.0 \text{ Ma}$ for Plešovice, and $562.6 \pm 1.2 \text{ Ma}$ for Piexé during the zircon analytical session, which are accurate to $\sim 0.2\%$, $\sim 0.4\%$, and $\sim 0.3\%$ of their reference values, respectively. For trace-element analyses, ^{90}Zr (assuming $\sim 43.14 \text{ wt. \% Zr}$) was used as an internal standard, with measured peaks on the 7700X at ^{27}Al , ^{28}Si , ^{31}P , ^{49}Ti , ^{51}V , ^{89}Y , ^{90}Zr , ^{93}Nb , ^{139}La , ^{140}Ce , ^{141}Pr , ^{146}Nd , ^{147}Sm , ^{153}Eu , ^{157}Gd , ^{159}Tb , ^{163}Dy , ^{165}Ho , ^{166}Er , ^{169}Tm , ^{172}Yb , ^{175}Lu , and ^{178}Hf . Iolite plug-in version 2.21 (Paton et al. 2011) for the Wavemetrics Igor Pro software was used to correct measured isotopic ratios and elemental intensities for baselines, time-dependent laser-induced inter-element fractionation, plasma-induced fractionation, and instrumental drift. Downhole fractionation was modeled using an exponential best fit. For all age and concordia calculations we used Isoplot v. 4.15 (Ludwig 2003).

Data were output for each integration recorded by the ICPMS systems. Profiles were manually screened for inclusions; Tables S2–S3 include all data, whereas Table S4 (and Fig. 7) includes only inclusion-free data. To calculate errors for each isotopic ratio on the Plasma 3D, we considered two sources of uncertainty: (i) laser stability throughout each shot and each run and (ii) measurement counting statistics at the detectors. The latter is important because the unknowns have significantly lower U, Th, and Pb than the secondary standards. To propagate laser-based uncertainties, we calculated the uncertainty in $^{238}\text{U}/^{206}\text{Pb}$ and $^{207}\text{Pb}/^{206}\text{Pb}$ required to make single age populations ($\text{MSWD} = 1$) for secondary RMs GJ1, Plešovice, and Piexé. Both laser and data sampling frequencies are 2 Hz, which ties each integration to each shot. Adding sufficient error to each 0.5-s integration individually requires $> 10\%$ individual errors in both

$^{238}\text{U}/^{206}\text{Pb}$ and $^{207}\text{Pb}/^{206}\text{Pb}$ for all standards; we, therefore, averaged every three integrations (~ 150 nm), requiring a more modest 7% error in $^{238}\text{U}/^{206}\text{Pb}$ and 2% in $^{207}\text{Pb}/^{206}\text{Pb}$ (added in quadrature). Adding Poisson counting uncertainties into each ratio magnifies the error in $^{207}\text{Pb}/^{206}\text{Pb}$ (12%) but does not significantly affect the $^{238}\text{U}/^{206}\text{Pb}$ error (8%), which reflects the minute Pb concentrations relative to U. $^{207}\text{Pb}/^{206}\text{Pb}$ -corrected $^{206}\text{Pb}/^{238}\text{U}$ dates were calculated using the Stacey and Kramers (1975) model $^{207}\text{Pb}/^{206}\text{Pb}_C$ for 50 Ma (0.83 ± 0.01). Propagating all in-run and decay-constant uncertainties into the date yields $\sim 7\%$ internal uncertainty in each reported U–Pb date. Long-term averaged external uncertainties from the UCSB lab are lower than this ($\sim 2\%$: Kylander-Clark et al. 2013) and thus we quote the internal uncertainty only. Because U and Th counts decrease linearly with increasing pit depth, these elements were corrected using a linear downhole fractionation model. Pb concentrations were calculated from downhole-corrected U concentrations using the assumed isotopic composition of U ($^{238}\text{U}/^{235}\text{U} = 137.818$; Hiess et al. (2012)) and the measured $^{238}\text{U}/^{206}\text{Pb}$, $^{207}\text{Pb}/^{206}\text{Pb}$, and $^{208}\text{Pb}/^{206}\text{Pb}$ (cf. Holder et al. 2019). Due to low ^{204}Pb counts, we do not report total Pb but rather report each Pb isotope abundance separately. Corrected $^{238}\text{U}/^{206}\text{Pb}$, $^{207}\text{Pb}/^{206}\text{Pb}$, U ppm, Th ppm, ^{206}Pb ppm, ^{207}Pb ppm, and ^{208}Pb ppm for primary and secondary RMs are shown in Fig. S1. Maximum Poisson-based uncertainties in U, Th, ^{206}Pb , ^{207}Pb , and ^{208}Pb ppm are 0.2%, 0.4%, 3%, 10%, and 4%, respectively.

A similar approach was taken for trace elements: 20–25% uncertainty is required to make M-HREE and Hf single populations for the secondary zircon standards, whereas counting statistics uncertainties are far lower than this (typically $< 5\%$). We recognize that the secondary zircon standards are not necessarily homogeneous with respect to trace elements, and thus we consider $\sim 20\%$ a conservative maximum error. Data for several elements with low counts or high internal errors (e.g., Ti, Nb, LREE) were discarded and not considered further.

Cathodoluminescence (CL)

Subsequent to depth-profiling analyses, the zircon mounts were polished to expose approximate central sections of the analyzed grains. CL images of these polished zircons were collected on a Cameca SX100 equipped with a Gatan Mono-CL detector at Rennselaer Polytechnic Institute, using a 15 kV accelerating voltage and a 12-nA beam current.

Raman spectroscopy

Raman spectra were collected on polished zircon grains using a Horiba LabRam HR Evolution Vis–NIR optimized & AIST-NT Scanning Probe at the Materials Characterization

Laboratory, Penn State. Spectra were excited using a 12-mW, 633 nm ultra-low frequency laser focused with a 50X microscope objective and a 25- μm confocal hole; the laser power was damped using neutral density filters to 50% of the maximum intensity at the sample surface. Raman-shifted light was diffracted using an 1800-groove/mm grating and collected with an electron-multiplying (EM) CCD detector. The machine was calibrated to an Si wafer (520.70 cm^{-1}) at the same conditions used to measure unknowns. Raman spectra shown in Fig. 9 are raw, uncorrected data; based on propagated uncertainties from laser, sample, and machine sources, and several repeat 12-h measurements of the Si wafer with varying detector windows, the error in any peak position is $\sim 0.3\text{--}0.4\text{ cm}^{-1}$. Raman spot analyses and linear transects were run on polished zircon grains with 2–3 accumulations of 10–60 s per spectral window, over the spectral range from $-400\text{--}1100\text{ cm}^{-1}$ (i.e., both Stokes and anti-Stokes shifts).

Field-emission scanning electron microscopy (FE-SEM)

FE-SEM images were collected on polished zircon grains using a Thermo Scientific Verios XHR Field-Emission Scanning Electron Microscope at the Materials Characterization Lab, Penn State. A 15-kV accelerating voltage and a beam current of 0.80 nA were used for all analyses; coarse images ($> 1\text{ }\mu\text{m}$ resolution) were performed in field-free mode, whereas finer images ($< 1\text{ }\mu\text{m}$ resolution) were performed in immersion mode.

Results

CL images

Zircons from fine-grained gabbro A01 have a sector-zoned, “soccer-ball” appearance with sharp boundaries between individual CL-bright and CL-dark zones (Fig. 2a); all grains have identical zoning. In contrast, zircons from coarser-grained samples B01 and C01 have CL-bright, sector- to oscillatory-zoned cores with uncommon, thin (typically $< 5\text{ }\mu\text{m}$, but locally up to $50\text{ }\mu\text{m}$), CL-dark rims (Fig. 2b–e). Some of the zircon cores show patches of extreme CL brightness that are unevenly distributed throughout the grain (e.g., Fig. 2d). Most zircons preserve at least one flat crystal facet, but exhibit lobate or pitted rims where the CL-dark zones preferentially occur (Fig. 2b, c). If present, CL-dark rims are often patchily distributed and only rarely mantle the entire grain; rims are thicker and more abundant in sample C01 than B01. Some rims exhibit oscillatory zoning, but it is not contiguous with similar zoning observed in the zircon cores (Fig. 2e).

Fig. 2 Cathodoluminescence (CL) images of zircon from M17X731A01 (a), M17S823B01 (b, c), and M17S823C01 (d, e). White bars in each figure are 50 μm (depth profile spot size) and blue bars are 15 μm (pit depths). Yellow arrows identify recrystallized, CL-dark metamorphic rims. Red lines in b, d indicate the location of the Raman spectroscopic transects in Fig. 9

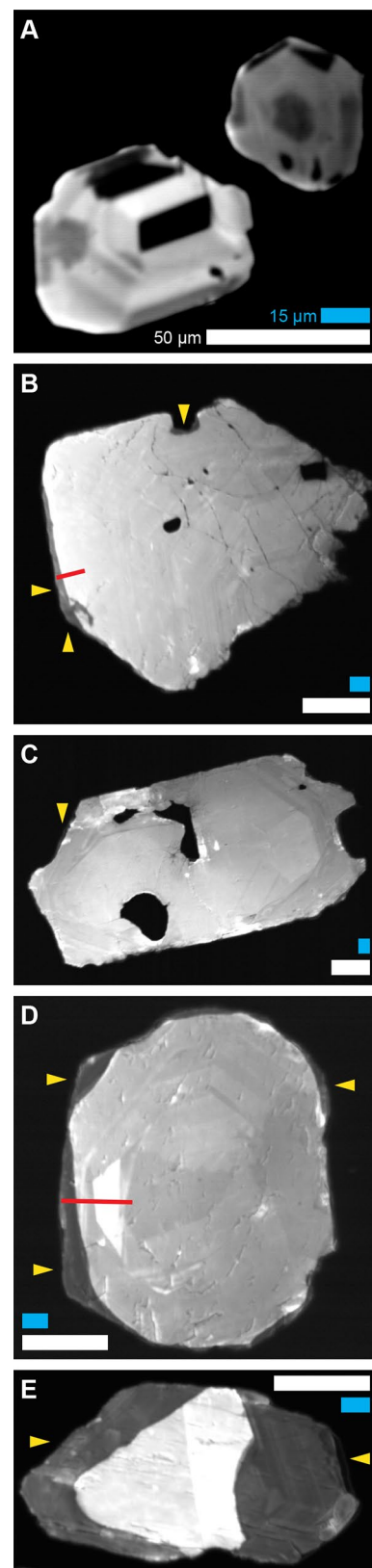
U–Pb and trace-element data

M17X731A01

Depth profiles from A01 ($n=23$) are homogeneous with respect to REE, Hf, and Th, with some zoning in U and Pb. U–Pb dates are within uncertainty across nearly all profiles, and Th/U is uniformly low (≤ 0.1). We therefore calculated integrated values for each profile before pooling the age and trace-element data for the entire population. These data are shown in Fig. 3 and Table S1. A least-squares fit discordia line through the data yields a U–Pb date of 50.2 ± 1.1 Ma (MSWD = 2.1) with a highly radiogenic upper $^{207}\text{Pb}/^{206}\text{Pb}$ intercept (~ 0.3). Fixing the upper intercept to the Stacey and Kramers (1975) model $^{207}\text{Pb}/^{206}\text{Pb}$ intercept at 50 Ma (~ 0.83) provides a statistically poorer fit that does not form a single population (MSWD = 3.1), but yields a U–Pb date within uncertainty of the unconstrained fit (51.6 ± 0.9 Ma). All spots exhibit flat, chondrite-normalized HREE slopes with low absolute REE abundances (Fig. 3, inset).

M17S823B01 and M17S823C01

Approximately sixty zircons were analyzed from each sample; representative, inclusion-free depth profiles are shown in Fig. 4. The complete dataset—with both inclusion-free and inclusion-bearing profiles—is contained in Tables S2–S3. From the edge to the interior of each zircon grain, the majority of depth profiles for both B01 and C01 exhibit the following: (i) a Hf-rich and U-, Th-, and REE-poor outermost rim that may exhibit either elevated or depleted total Pb relative to the rest of the grain; (ii) an increase in U, Th, and REE and a decrease in Hf inward of the outermost rim; (iii) a peak or plateau in U, followed by an exponential decrease in U toward the grain core; and (iv) a sharp knick-point in slope for all other elements at or slightly inward of the U peak, followed by flat or smoothly varying profiles toward the grain interior (Fig. 4a–d). Uranium abundances are heterogeneous among grains, with average concentrations ≤ 40 ppm for zircon cores and up to ~ 200 ppm at U peaks. Th/U mirrors the behavior of U, smoothly increasing from ~ 0.1 to ~ 0.5 – 0.6 over the rim-to-core interval, and reaching a plateau along the flattest portion of the U profile. Though most Th profiles roughly parallel other trace-element distributions, rare Th profiles show exponentially increasing or decreasing concentrations from rim to core (e.g., Fig. 4d).



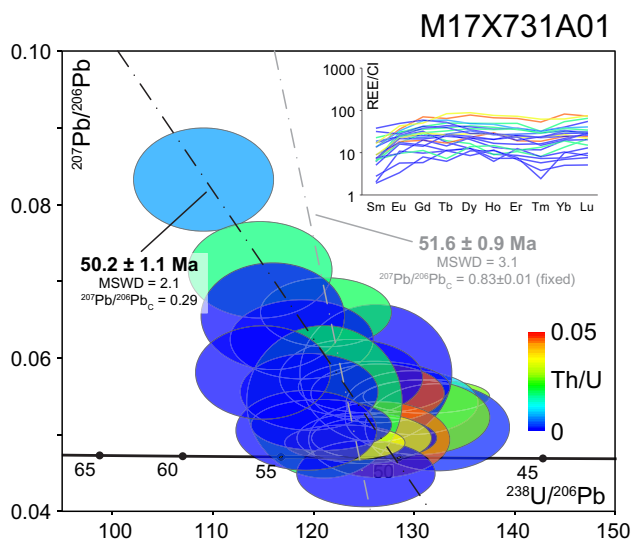


Fig. 3 Tera-Wasserburg concordia figure and chondrite-normalized REE data for zircons from a fine-grained, foliated, eclogitic Fe-Ti metagabbro (M17X731A01; cf. Fig. 2a). Two isochrons are shown, the first with an unconstrained upper intercept that is a better statistical fit to the data (black), and a second calculated using a fixed $^{207}\text{Pb}/^{206}\text{Pb}$ intercept of 0.83 ± 0.01 (gray; as in Fig. 4). Zircons from this sample yield a single age and trace-element population consistent with eclogite-facies growth

Lead frequently exhibits linear or gently curved profiles that generally mimic U (^{206}Pb , ^{207}Pb) and Th (^{208}Pb) variations. In contrast, trace elements are more systematic, with flat, gently sloping, or concave-down rim-to-core profiles mantled by abrupt rim decreases (P, REE) or increases (Hf). The outermost rims typically have lower total REE concentrations, higher Dy/Yb, and higher Eu/Eu*. The rims defined by all elements except U are typically only a few microns thick, whereas U exponentially decreases to a minimum over longer scales (up to 15 μm). Rare grains exhibit thicker rims that occupy the entirety of the depth profile (i.e., > 15 μm). Such rims (Fig. 4e) have elemental abundances (high Hf, low P-REE-Th) and U–Pb dates (exclusively ~ 50 Ma; see below) that match thinner rims on other grains, and exhibit complex U zoning—either increasing or decreasing toward the core—with unzoned trace elements. Another set of rare profiles (e.g., Fig. 4f) has solely old U–Pb dates (~ 160 Ma) with elevated trace-element concentrations matching other zircon cores; no elements in these profiles are zoned.

$^{207}\text{Pb}/^{206}\text{Pb}$ -corrected $^{206}\text{Pb}/^{238}\text{U}$ dates were calculated for each integration by fixing the upper intercept to the Stacey and Kramers (1975) value for 50 Ma (0.84 ± 0.01). The resulting profiles yield continuous U–Pb arrays from rim to core, typically mimicking the Th/U topology. $^{208}\text{Pb}/^{232}\text{Th}$ dates for the same profiles are highly imprecise (e.g., ± 100 s of Ma) and thus cannot resolve core-rim age differences in any grains. To identify endmembers from the profiles, we

first examined each profile separately, and extracted U–Pb isochron (rim) or weighted-mean dates (cores) and average trace-element concentrations for rim and core single age populations (MSWD ~ 1). Results are shown in Fig. 5. Figure 5a shows that—even for U–Pb isochrons and weighted means defined by ≥ 10 integrations (≥ 15 s, or ≥ 1.5 μm)—there is a discontinuous spread in calculated date from ~ 160 Ma to nearly ~ 45 Ma. These trends are matched by a gradual evolution in trace-element composition (Fig. 5b) with lower Th/U, lower total REE, and a more positive Eu anomaly for ≤ 65 Ma zircon. Many intermediate U–Pb dates occur in zircon cores that have single-population U–Pb dates and are homogeneous with respect to trace elements. For example, Fig. 4a–d shows profiles with broad core zones (~ 5 μm) with flat age and trace-element zoning, but systematically younger dates (~ 135 Ma) than the established Tethyan igneous crystallization age for the Monviso metagabbros (163 ± 2 Ma; Rubatto and Hermann 2003; Rubatto and Angiboust 2015). Likewise, rim isochrons among low Th/U-spots yield apparent dates as old as ~ 80 Ma – significantly older than garnet-whole rock Lu–Hf (Duchêne et al. 1997) and U–Pb zircon dates (Rubatto and Hermann 2003; Rubatto and Angiboust 2015) that indicate metamorphism at ~ 50–45 Ma.

To more precisely determine the mechanisms and timing of rim age resetting, we compiled aggregate depth-profiling data for samples B01 and C01. This compilation includes all data used to calculate the rim and core dates in Fig. 5 as well as all inclusion-free depth profiles, resulting in $n = 2550$ integrations for B01 and $n = 2770$ for C01 (see Table S4 for compiled data). The compositional data are plotted against U–Pb date—serving as a normalized proxy for profile depth—in Fig. 6. Though there is significant scatter with numerous outliers, the amassed trace-element data indicate apparent two-component mixing, with points hyperbolically distributed between endmembers. Th/U and total REE (using Y as a proxy) generally decrease and Dy/Yb and Eu/Eu* generally increase toward grain rims, whereas Th/U decreases semi-continuously over the range of measured U–Pb dates, Y, Dy/Yb, and Eu/Eu* are similar for most dates and only change in the youngest population. A more extreme young compositional endmember is also observed in sample C01 compared to sample B01, as Th/U and Y are lower and Dy/Yb is higher for the ~ 50 Ma population, whereas Eu/Eu* follows a similar pattern in both samples. In contrast, the compiled U, Th, and Pb data exhibit more complex trajectories: with decreasing date, U concentrations increase to a maximum (≤ 200 ppm) at ~ 50 Ma, followed by a decline to lower values (~ 10 ppm) at the same date. Thorium likewise increases (sample B01) or decreases (sample C01) at ~ 50 Ma but is otherwise uncorrelated with U–Pb date, and exhibits similar concentrations over the age array. The abundances of ^{206}Pb and ^{207}Pb are flat or increase gently from core to rim (cf. Fig. 4a–d), whereas ^{208}Pb does not

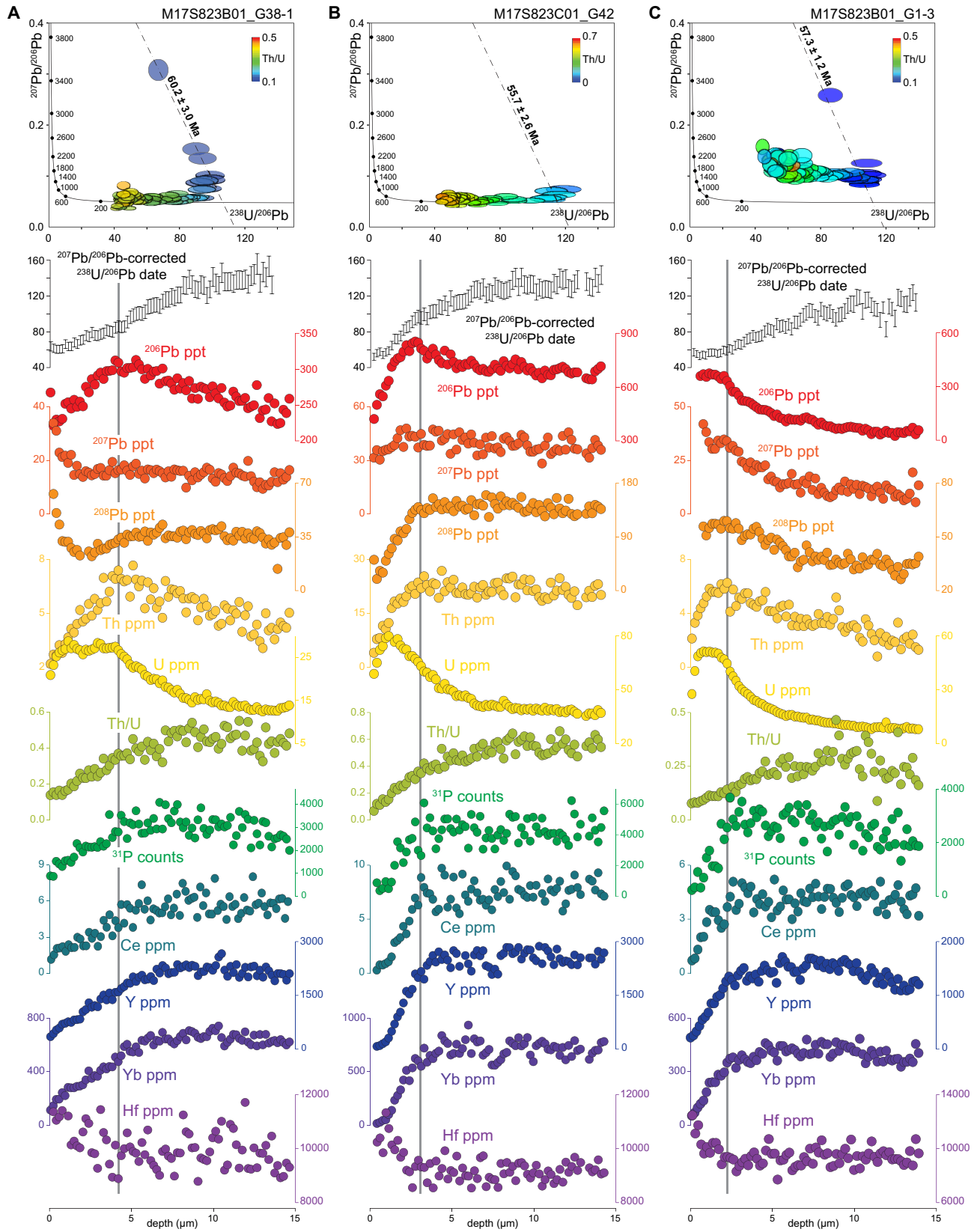


Fig. 4 Selected LASS depth profiling results from coarse-grained Fe-Ti metagabbros M17S823B01 and M17S823C01. Each column represents a ~15 μm depth profile from a single grain. $^{207}\text{Pb}/^{206}\text{Pb}$ -corrected $^{206}\text{Pb}/^{238}\text{U}$ dates (including all isochron dates in the first row of the figure) were calculated using a fixed $^{207}\text{Pb}/^{206}\text{Pb}$ intercept of 0.83 ± 0.01 . Profiles **a–c** represent relatively typical depth profiles with sharp core-rim boundaries in trace elements and more gradual U and U–Pb age changes over the same interval, whereas profile **d** shows similar features but with an exponentially decreasing Th profile from rim to core. The distribution of isotopic data above concordia in profile **c** likely results from initial common Pb in the zircon core.

vary significantly; however, the youngest population exhibits increases (B01 and C01) and decreases (C01 only) in all Pb isotopes relative to cores.

Notably, sample C01 exhibits a U-, Th-, and REE-poor, high Dy/Yb-Eu/Eu* zircon population that is less apparent in sample B01 (Fig. 6). These data exhibit the flattest chondrite-normalized REE patterns and consistently youngest U–Pb dates (Fig. 7a). Isolating this population yields a single-population isochron date (51.1 ± 0.4 Ma; MSWD = 1.2, $n=96$) (Fig. 7b) within uncertainty of that from sample A01 (Fig. 3).

Diffusion modeling

Remarkably, once profiles with obvious mineral inclusions are filtered from the dataset, the U concentration profiles observed in samples B01 and C01 (e.g., Fig. 4) resemble stranded diffusion profiles observed in natural metamorphic crystals, in which elements liberated during resorption partition back into the relict crystal and drive inward diffusion (e.g., Carlson 2012). Even those profiles that contain inclusions show similar, apparently diffusive topologies in their inclusion-free portions. Similar U profiles are obtained experimentally for zircon implanted in U-rich media that underwent no resorption (Cherniak et al. 1997a). If the measured U concentration profiles arise from inward diffusion, such diffusion must be fundamentally different than that measured experimentally; using the activation energy (726 ± 83 kJ/mol) and pre-exponential constant (0.212 ± 2.440 m²/s) from Cherniak et al. (1997a) for U diffusion in zircon yields characteristic length scales of ≤ 1 fm ($\leq 10^{-15}$ m) for 1–10 My at 550 °C, whereas apparent diffusive length scales observed here are up to ~10–15 μm and are similar between grains.

To estimate the diffusivity of U through zircon required to account for the observed depth profiles, we first took the approach of Stearns et al. (2016) and modeled isotropic, constant-diffusivity, tracer diffusion into a semi-infinite medium with a constant rim U concentration and a uniform initial U concentration in the host zircon. This fixed-boundary approach models the endmember case of external addition of U to zircon grain boundaries and provides a

Gray bars behind compositional data in **a–d** represent the location of rim–core transitions observed in P and Ce. In contrast, profiles **e, f** show single age populations (**e**=entirely metamorphic, **f**=entirely igneous) and lack clear core–rim relationships, although there is some U zoning in profile **e**. Because counts-based uncertainties (~3–4% for ^{206}Pb and ^{208}Pb , ~10% for ^{207}Pb , ~0.2% for U, ~0.4% for Th) may be underestimates, and depth profiling data are not exported with uncertainties, we show the raw data only; however, we note that the scatter in individual profiles gives a rough estimate of the precision of each elemental analysis

first-order constraint on the diffusivity using the observed length scale over which U profiles vary. Diffusion coefficients were calculated from normalized concentration profiles using the following analytical solution to the diffusion equation (Crank 1975):

$$\text{erf}^{-1}\left(\frac{C_x - C_r}{C_c - C_r}\right) = \left(\frac{1}{\sqrt{4Dt}}\right)x.$$

in which x is position, C_x is the concentration at position x , C_c and C_r are endmember core and rim concentrations, respectively, t is time, and D is the diffusivity. The raw U concentration profiles used in the inversions are shown in Fig. 8a, b; note the similarity in length scales of curvature between profiles with different U concentrations. All apparently inclusion-free profiles that captured the full rim-to-core compositional changes were compiled for the calculation, and only the portions of the profiles inward of each U spike—where U decreases occur in the absence of any other compositional changes (Figs. 4, 6, and 7)—were considered (Fig. 8a, inset). Endmember rim and core U concentrations were chosen for each profile using the peak U concentration and the minimum U concentration in the deepest part of the profile, respectively. D_U was calculated for each grain from the slopes of the erf^{-1} inverted profiles (Fig. 8c, d), which are proportional to $D^{-0.5}$. We used $t=1$ My to calculate D based on the evidence in this (see Discussion) and other studies (Rubatto and Angiboust 2015; Broadwell et al. 2019) for ~1–2 My peak metamorphic timescales. Using 10 My timescales reduces the calculated diffusion coefficients by an order of magnitude, whereas using shorter timescales increases them.

The first few microns inward of the U peak have higher inverted profile slopes (=lower D_U) relative to more homogeneous grain interiors. This is observed in every measured grain regardless of U concentration, and occurs in regions outboard of the sharp trace-element rim, where U concentrations are highest. Using the homogeneously sloped portions of the inverted profiles, the calculated average D_U for the two samples is identical within uncertainty ($D_U \sim 10^{-24}$ m²/sec). Stated uncertainties in D_U in Fig. 8c, d (cf. Fig. S2–S3 for individual profile fits) are two standard deviations of the

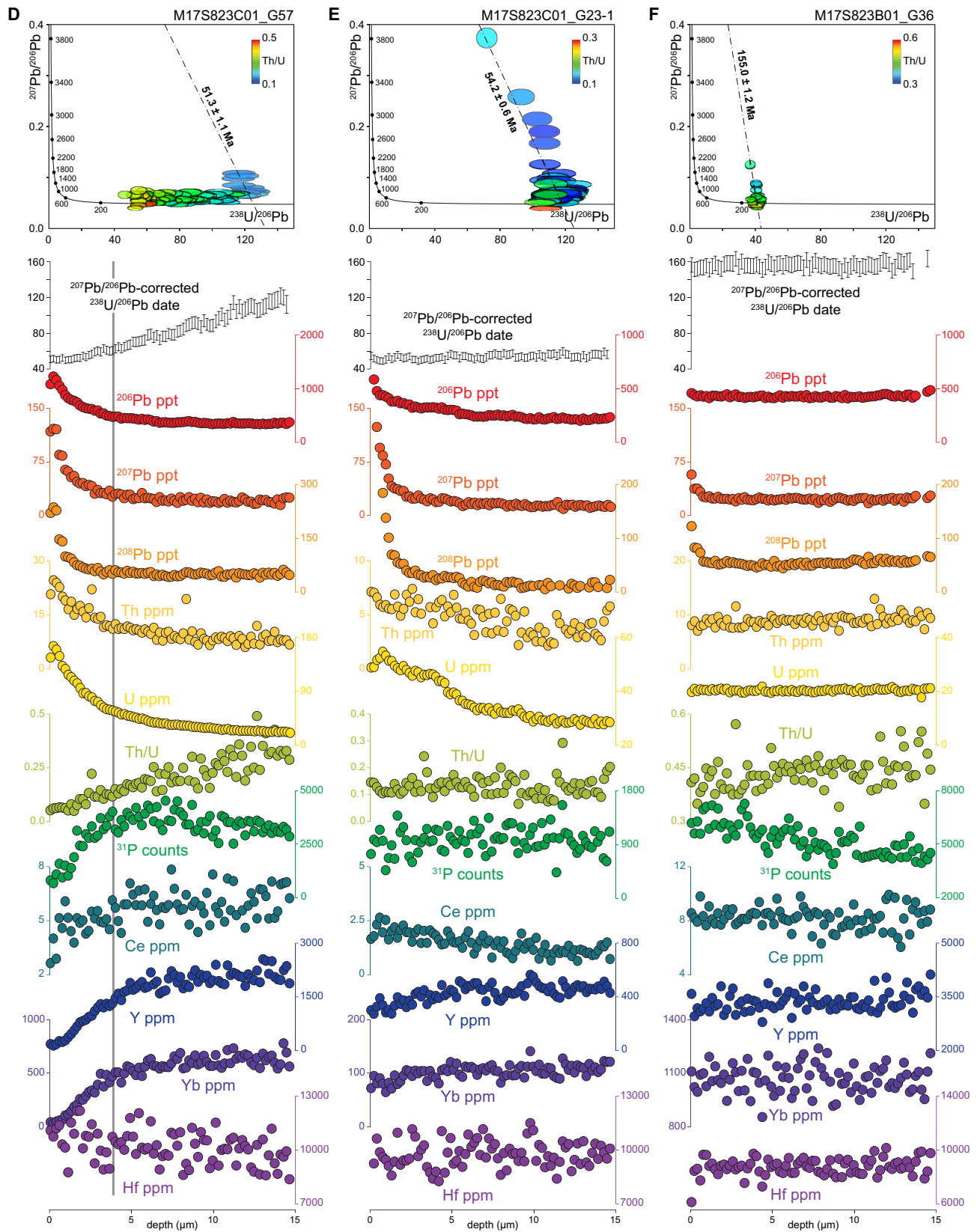


Fig. 4 (continued)

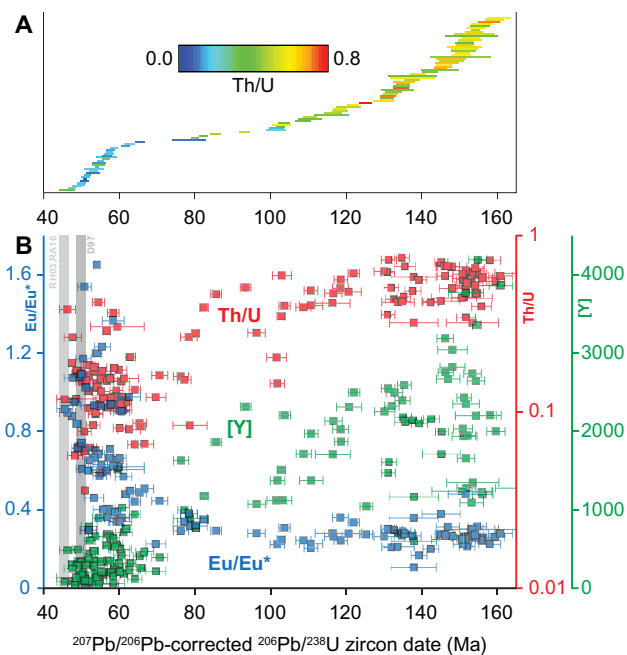


Fig. 5 Compiled isochron and weighted mean data for samples M17S823B01 and M17S823C01; see Tables S2–S4 for raw data. Isochrons were calculated for rim zones in which sequential laser shots yielded single, Stacey and Kramers (1975) corrected $^{207}\text{Pb}/^{206}\text{Pb}$ -corrected $^{206}\text{Pb}/^{238}\text{U}$ age populations. Weighted mean dates were likewise calculated for zircon cores with obvious age plateaus; these were not calculated as isochrons due to the limited spread in $^{207}\text{Pb}/^{206}\text{Pb}$. **a** Ages and Th/U recorded by samples with isochrons defined by more than 30 integrations ($\sim 1.5\ \mu\text{m}$). The data form a continuous spread of both protolith and metamorphic dates, with metamorphic trace elements occurring for dates from ~ 60 to 50 Ma. **b** Th/U, Y, and Eu/Eu* zircon averages for all isochron and weighted mean dates, with a notable shift in composition at ~ 60 –65 Ma. The gray bars denote Lu–Hf garnet dates (D97: Duchêne et al. 1997) and U–Pb zircon dates (RH03: Rubatto and Hermann 2003; RA15: Rubatto and Angiboust 2015) determined for Monviso metagabbros

sample-averaged D_U ; Poisson-based counting uncertainties in U concentration are negligible ($\sim 0.2\%$) and thus uncertainties in individual slope fits are far higher than the uncertainty on the average.

Recognizing the abundant textural and chemical evidence for zircon resorption (Figs. 2, 4), we performed an additional coupled diffusion–dissolution model, following the kinetic model presented in Smye et al. (2017). Our model solves the conservative form of the diffusion equation, discretized across the radial dimension of an individual zircon crystal:

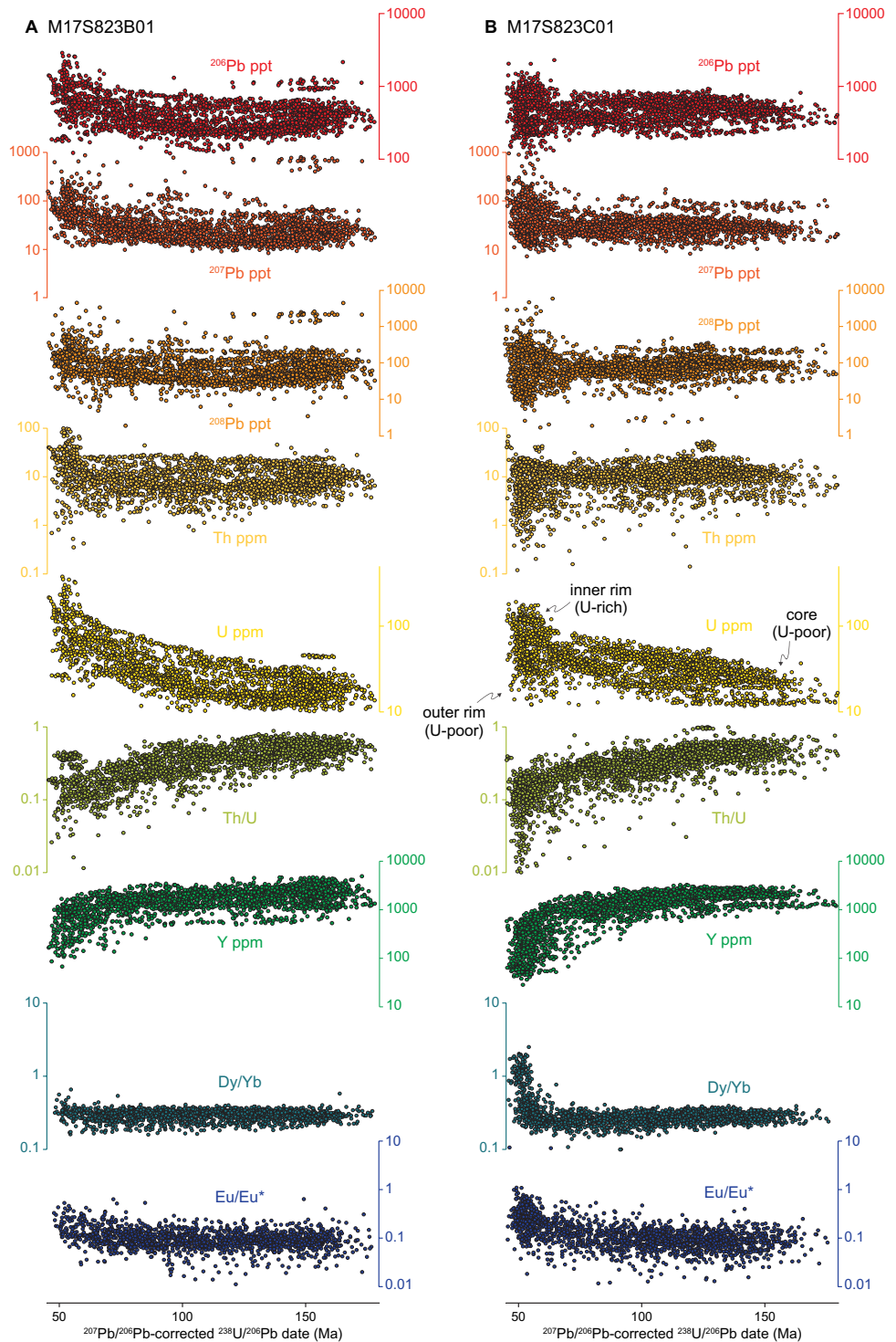
$$\frac{\partial}{\partial t} (r_j^\gamma C_s^i) + \frac{\partial}{\partial r} (r_j^\gamma F_c C_s^i) = 0 \text{ on } \Omega_s \in [r_{\min}, R] \times [0, t_j],$$

in which r_j is the radial index, R is the crystal radius, t_j is the time index, C_s^i is the concentration of U in the zircon, and γ reflects the radial dependence of volume and area in

cylindrical and spherical coordinates; γ was set as 1 (cylindrical) for all calculations in this study. The terms $r_j^\gamma C_s^i$ and F_c represent the accumulation and diffusive flux of U, respectively. A Neumann symmetry condition was implemented at the crystal center ($r_j = r_{\min}$), whereas a mass-balance partitioning constraint was employed at the crystal interface ($r_j = R$), accounting for both dissolution and diffusion of U between zircon and a grain boundary fluid reservoir of fixed volume. Zircon dissolution was implemented by re-gridding at each timestep, conserving the number of cells, and motion of the interface was simulated using a power-law relation ($n=2$). We assumed the same timescales for dissolution and diffusion ($t=1\ \text{My}$) as for the fixed-boundary model (above), with dissolution assumed to propagate in even steps over this duration. The relevant equations were solved numerically using a fully implicit finite-volume discretization, following the approach presented in Hesse (2012). Goodness of fit was assessed using the L2 norm (root sum of squared residuals) between observed and modeled profiles, run over a grid of D_U and initial zircon radii for each profile, the residual output over the minimization grid forms an error ellipse with significant covariance (cf. Fig. S4), reflecting a correlation between the amount of zircon dissolution and the required rate of U diffusion to match the depth profiles.

Several other variables serve as inputs for the calculation, and parameter sensitivity tests were performed for the most uncertain of these. Final zircon radii were measured directly from the unpolished zircon mounts, with the shortest dimension used for the calculation. Initial U concentrations in zircon cores were determined from the minimum U concentration in each depth profile; varying this parameter affects the predicted amount of zircon resorption by $\leq 20\ \mu\text{m}$, but has a negligible effect on the calculated D_U . Uranium was assumed to strongly partition into zircon ($K_d \gg 1000$) to match the observed length scale of resorption features and metamorphic rims in CL images of our samples (~ 2 – $20\ \mu\text{m}$; e.g., Fig. 2). Experimental zircon/fluid partition coefficients are significantly lower than this (~ 1 : Ayers and Peters 2018), but these experiments were run at slightly more oxidized conditions (NNO buffer) than our samples likely experienced (QFM buffer; see Discussion). Although changing the zircon/fluid $K_d(\text{U})$ to the experimental values has a significant effect on the amount of zircon resorption required to match the profiles by several hundred microns—yielding an unrealistic initial zircon size—it has little effect on the calculated D_U (Fig. S4). Therefore, our use of an extreme zircon/fluid K_d should be considered as the endmember case in which all U is sourced from pre-existing zircon, in contrast to the fixed-boundary model (above) in which

Fig. 6 Aggregate Pb, Th, U and trace-element data vs. Stacey and Kramers (1975) $^{207}\text{Pb}/^{206}\text{Pb}$ -corrected $^{206}\text{Pb}/^{238}\text{U}$ date for each zircon integration from M17S823B01 (**a**; $n=2550$) and M17S823C01 (**b**; $n=2770$). Each datum represents the average of three integrations (approximately three laser shots). Data were extracted from all inclusion-free depth profiles, and all points used to construct the isochron data in Fig. 5 (i.e., inclusion-free portions of inclusion-bearing profiles; see Table S4 for raw data). The youngest dates (left) correspond to rims in depth profiles, whereas the oldest dates (right) correspond to cores. Endmembers identified in the text are marked in the U data for C01. Note that—although each sample shows a similar trace-element vs. age evolution—C01 shows a more significant transition to eclogite-facies U-Th-Pb and trace-element signatures



all U is sourced externally. Parameter sensitivity tests on other model variables (dr , dt , grid spacing for the minimization routine, etc.) yield slight changes in model fits, but ultimately result in variations in D_U that are less than one-tenth of an order of magnitude.

Results from this model are shown in Fig. 8e–f, with individual profile fits in Figs. S5–S6. As for the

fixed-boundary model, stated uncertainties in D_U are two standard deviations of the sample-averaged D_U . The calculations suggest almost identical but slightly higher diffusivities to those calculated with the fixed-boundary model, and both samples are within uncertainty of each other, reflecting the nearly congruent length-scales of diffusion required for small fractions of resorption. The

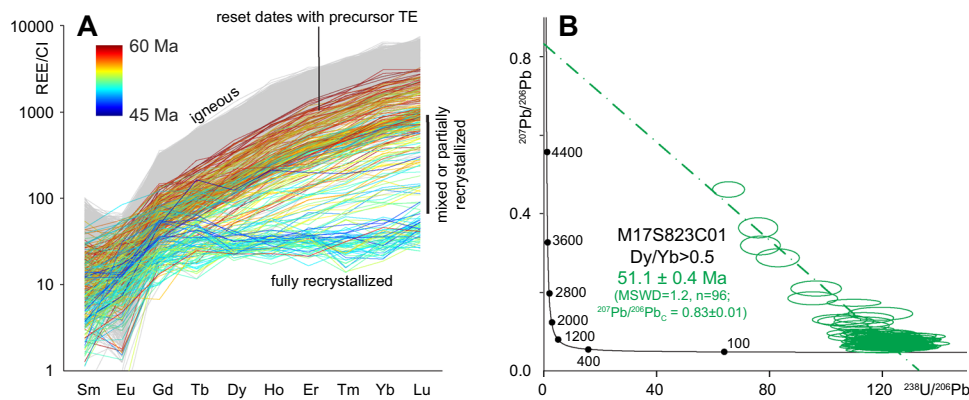


Fig. 7 **a** Chondrite-normalized zircon REE profiles colored by U–Pb date for M17S823C01. All spots > 60 Ma exhibit positive MREE–HREE slopes, a pronounced negative Eu/Eu* anomaly, and are shaded gray. ~60 Ma dates exhibit also exhibit positively sloping HREE, but with lower REE abundances and more modest Eu/Eu* anomalies; these data transition abruptly to spots with ~50 Ma U–Pb

dates, flat HREE slopes, and low U concentrations. **b** Tera-Wasserburg concordia plot with only the most HREE-depleted zircon data from M17S823C01. A $^{207}\text{Pb}/^{206}\text{Pb}$ -corrected $^{206}\text{Pb}/^{238}\text{U}$ discord through these data—anchored to Stacey and Kramers (1975) common Pb (0.83 ± 0.01)—yield a single-population U–Pb date

range of model results obtained in this study are displayed in Fig. 8g relative to those obtained experimentally by Cherniak et al. (1997a), extrapolated to the temperatures experienced by our samples (Angiboust et al. 2012b).

Raman data

Core-to-rim Raman spectroscopic transects on sample B01 and C01 were performed to determine the role of zircon lattice damage on the compositional results. Transects were done over recrystallized rim boundaries and CL-bright grain edges without CL-dark rims, and extended over scales relevant to pit depths ($\leq 15 \mu\text{m}$; see Fig. 2 for representative transect locations). Equant, sector-zoned zircons from M17X731A01 were analyzed for comparison.

Representative Raman data are shown in Fig. 9, with spot data from different grains in M17X731A01, and transects from M17S823B01 and M17S823C01. Measurements from all samples show several diagnostic peaks from unmodified crystalline zircon, including stretching modes at ~ 1008 and $\sim 975 \text{ cm}^{-1}$ and bending modes at ~ 439 and $\sim 356 \text{ cm}^{-1}$ (Nasdala et al. 1995; Zhang et al. 2000; Kolesov et al. 2001; Schmidt et al. 2013). The relative intensity of each peak varies between grains from a single sample, but all measured zircons (regardless of sample) exhibit the same peak positions. There are no significant changes along any of the core-to-rim transects; each rim spectrum exhibits nearly congruent peak positions and widths with their associated cores. Several grains—including whole grains from M17X731A01 and zircon cores from M17S823C01—exhibit a weak, narrow peak at $\sim 640 \text{ cm}^{-1}$ and a broader band at $\sim 820 \text{ cm}^{-1}$ that always occur in concert with each other. Though the $\sim 640 \text{ cm}^{-1}$ peak can result from tetragonal ZrO_2 formed

after metamict zircon (Zhang et al. 2000), other peaks associated with this phase are not observed, and a weak band observed at 641 cm^{-1} may arise from an additional zircon bending mode (Kolesov et al. 2001).

FE-SEM data

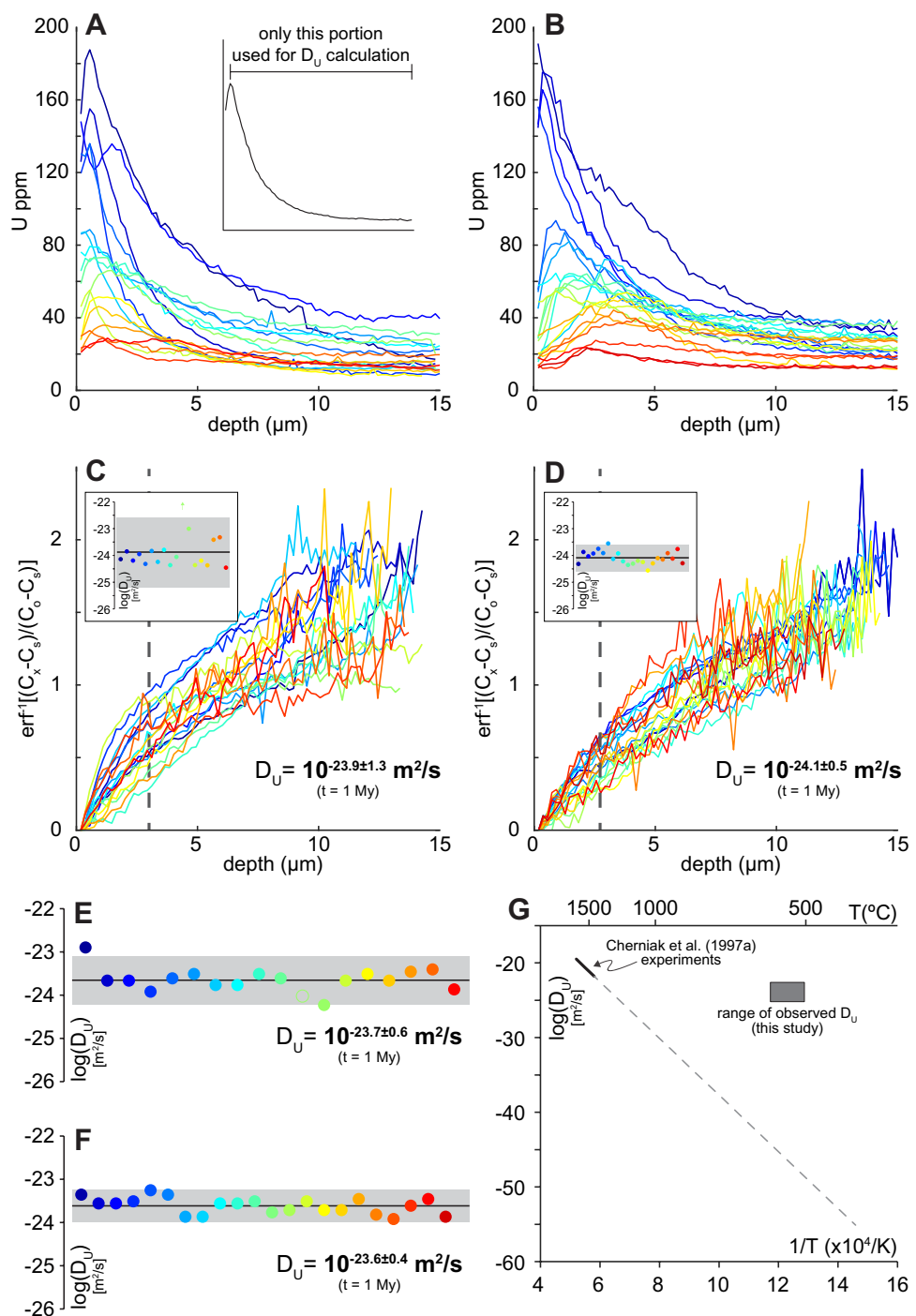
High-resolution FE-SEM images—including secondary-electron and backscattered-electron images—were collected to determine the potential role of micro- to nano-scale fracturing or porosity in explaining the observed U profiles, particularly because these features are often present in dissolved and reprecipitated zircon (e.g., Geisler et al. 2007). The imaging was performed for the same textural settings and length scales ($\sim 5\text{--}50 \mu\text{m}$) analyzed by depth profiling and Raman spectroscopy, including the same zircons for which Raman data are presented in Fig. 9. These images are presented in Figs. S7–S8. Although there are minor cracks and pits related to polishing, these are randomly distributed and none are geometrically associated with grain or reaction boundaries. Additionally, there are no observable pores at any scale.

Interpretations and discussion

Discriminating distinct zircon populations and processes

The laser-ablation, CL, and Raman data indicate several zircon populations among the three samples. The salient features of each of these are reviewed with the intent of

Fig. 8 Zircon U profiles from M17S823B01 (a) and M17S823C01 (b), with accompanying fixed-boundary inversions (c = B01, d = C01) and moving-boundary, coupled dissolution-diffusion modeling results (e = B01, f = C01) for uranium-in-zircon diffusivity for the same transects; colors in (a, b) correspond to those in (c, d, e, and f). The inset in a shows the selected portions of the profiles in a and b used to calculate D_U in all models. The insets in (c, d), and the entirety of panels (e, f), show the calculated D_U for each individual profile, with the calculated average and 2 SD in a black line and gray box, respectively. The black dashed lines in (c, d) delineate higher slopes (diffusivities) in the fixed-boundary model towards the rim of zircon grains. g plots the observed results from this study (gray box) relative to those obtained in high-temperature experiments (Cherniak et al. 1997a), with the range of measured data in black and extrapolation to low- T as a gray dashed line. See text for additional calculation details, and Figs. S2–S3 and S5–S6 for individual fixed-boundary and moving-boundary model fits superposed on the raw data



connecting compositional, textural, and mineralogical data; a graphical summary of this discussion is shown in Fig. 10.

A01: metamorphic neocrystallization

The equant, sector-zoned zircons in sample A01 (Fig. 2a) constitute a population separate from zircons in the other two samples. These zircons typically have high U (> 100 ppm) with HREE-depleted trace elements compatible with a

garnet signature (Rubatto and Hermann 2007; Taylor et al. 2017). We interpret these zircons as neocrystallized eclogite-facies metamorphic grains. M17X731A01 occupies a structural position distinct from the other two samples; it was collected from the core of the LSZ, which experienced significant eclogite-facies metasomatism (Angiboust et al. 2011, 2014). The distinct textures and geologic context thus indicate that these zircons precipitated from the metamorphic fluid at 50.2 ± 1.1 Ma. Though the Tera-Wasserburg

discordia upper intercept for these zircons ($^{207}\text{Pb}/^{206}\text{Pb} \sim 0.3$) is more radiogenic than the Stacey and Kramers (1975) value for ~ 50 Ma ($^{207}\text{Pb}/^{206}\text{Pb} \sim 0.84$)—potentially suggesting Pb^* inheritance from a precursor U-bearing phase – there is no textural evidence for this in the zircon CL images. If present, any such phase was entirely resorbed prior to or during the Alpine event.

B01 and C01: igneous cores

Most depth profiles through B01 and C01 zircons sample an endmember consistent with igneous crystallization in the protolith gabbro (Fig. 10). We restrict our interpretation of these cores to zones with flat age and trace-element plateaus in the deepest part of the profiles; zones with continuously varying age are discussed below. This endmember is richest in REE with the lowest Dy/Yb, the highest Th concentrations with Th/U up to 0.6, and a pronounced negative Eu anomaly (Figs. 4, 6). Rubatto and Hermann (2003) and Rubatto and Angiboust (2015) identified protolith zircons with similar trace-element signatures, and measured a crystallization date of 163 ± 2 Ma. Though some zircons were clearly altered, other zircon analyses on visibly unaltered grains exhibited partially reset dates (≤ 80 Ma) but with unmodified protolith $\delta^{18}\text{O}$ (Rubatto and Angiboust 2015). Likewise, though the zircon cores analyzed here form flat age plateaus with no apparent evidence for U–Pb, trace-element, or structural (cf. Fig. 9) modification, only some of the single-population weighted mean dates for zircon cores match the 163 ± 2 Ma igneous crystallization date (e.g., Fig. 4f). Dates for similar Alpine Tethyan gabbros range between ~ 170 and 150 Ma across the Western Alps and Corsica (Manatschal and Müntener 2009; Li et al. 2015) but homogeneous zircon core dates in this study are as young as ~ 80 Ma. Notably, these younger dates occur even for cores with nearly homogeneous U concentrations, in contrast to the asymptotic profiles developed toward grain edges. However, it is possible that minute U increases affected even the deepest parts of most of our ~ 15 μm depth profiles; for an igneous zircon that crystallized at 163 Ma with 15 ppm U (the average core concentration measured in our study), the addition of 1–2 ppm U is sufficient to alter U–Pb dates by 5–15 My. Finally, rare profiles with exclusively old U–Pb dates (Fig. 4f) show nearly flat U concentration profiles. Because the maximum counting statistics uncertainties on U using our methods are exceedingly low (0.2%), these data suggest that magmatic zircon was not zoned in U at the sub-ppm level.

B01 and C01: igneous cores with U–Pb dates reset by U gain \pm recrystallization

Several noteworthy changes are recorded within ~ 5 μm of grain rims. From core to rim, trace elements remain

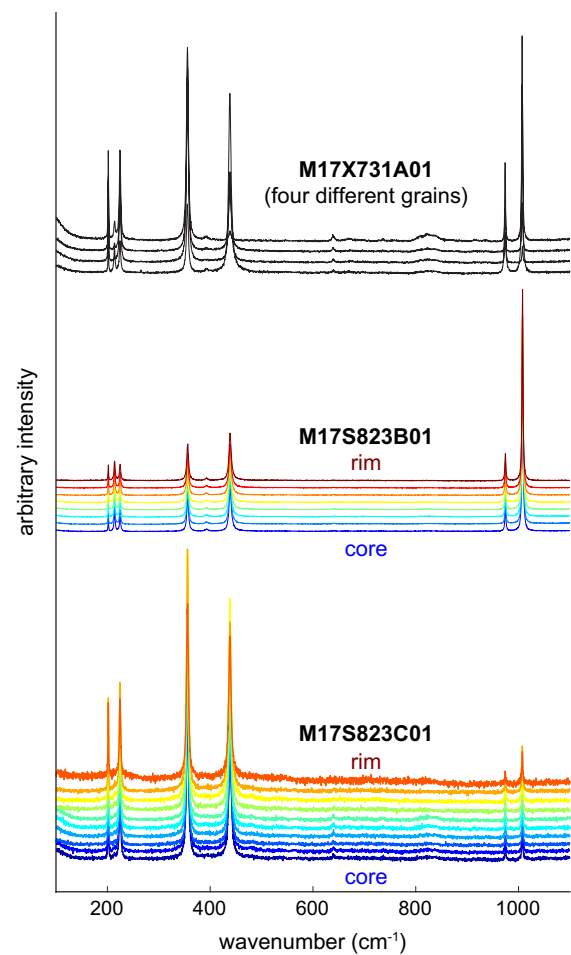


Fig. 9 Zircon Raman spectra (see Table S2 for data). Top four spectra are from multiple grains in M17X731A01; lower two sets of colored spectra are core-to-rim transects across the grains in Fig. 2b (M17S823B01; middle) and Fig. 2d (M17S823C01; bottom). Though there are slight differences in peak intensity across each spectrum, there are no differences in peak position or width among or within samples, or from zircon cores to rims

relatively homogeneous but U achieves a maximum, Th/U and U–Pb date are progressively reset toward ~ 0.1 and ~ 50 Ma, respectively, and there is typically REE and P loss with Hf gain where U concentrations are highest (e.g., Figs. 4, 10). Though some outer zircon rims appear to contain Pb_c increases, and are more discordant in Tera-Wasserburg space (Figs. 4, 6), others show decreases in all Pb isotopes, suggesting radiogenic Pb^* loss. Likewise, some profiles show Th decreases while others show increases, and rare profiles show similar diffusion-like Th profiles to U (e.g., Fig. 4d). Given the location of this material in the depth profiles, it likely represents material straddling the CL-bright and CL-dark boundaries.

The synchronicity and sharpness of the rims defined by all elements excluding U (Figs. 4, 10) suggest that the trace-element knickpoint in each profile is a frozen

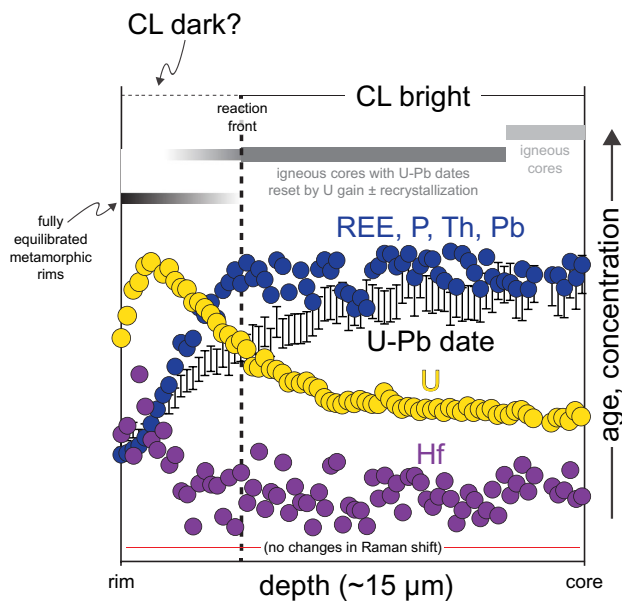


Fig. 10 Summary of textural, compositional, and mineralogical data from the zircon depth profiles, based on data from Fig. 4b. The labels for each zircon textural occurrence match the sequence in the “Discussion” section

reaction boundary, attained during fluid-induced dissolution of the grain rim. Resorption textures are apparent in the CL data and include pitted, concave grain boundaries and truncated core zoning. Further, both samples contain hydrated eclogite-facies minerals (e.g., phengite, talc, chlorite, former lawsonite) testifying to fluid-present conditions during peak metamorphism. According to this interpretation, material rim-ward of the reaction boundary was recrystallized or reprecipitated, whereas material core-ward of the reaction boundary appears to have faithfully preserved most protolith trace elements (excluding U). The loss of REE, P, and sometimes Pb and Th suggests that these elements were partitioned into the fluid or into other metamorphic phases (e.g., allanite, monazite); more uncommon profiles with Pb or Th increases at the grain rim suggest the additional influence of local equilibrium.

In contrast, the correlated and population-wide rim-to-core evolution of U, Th/U, and U–Pb date is compatible with inward U diffusion ahead of the reaction front, leading to an exponential array of ages without systematically affecting other elements. In interpreting that the U profiles arise are diffusive, we acknowledge that there are several non-diffusive processes that could theoretically produce similar U topologies. Each of these is addressed below:

1. *Downhole fractionation corrections* Incorrect modeling of downhole inter-element fractionation could yield U profiles conforming to an error function. However, the secondary zircon reference materials—measured and

treated identically to unknowns—yield flat U, Th, and Pb concentration profiles (Fig. S1), suggesting no obvious errors in our downhole correction method.

2. *Analytical mixing* Mixing during laser-ablation analysis—either along a curved or tortuous core-rim boundary, or by previously excavated or laser pit wall material falling back into the laser pit—is unlikely for several reasons. First, simple mixing models (Fig. S9) can test the influence of a curved core-rim boundary on depth-profile elemental topologies. The models show that although there are geometric configurations that could produce the observed U profile, such mixing would be resolvable in any other species that differed in concentration between the core and rim, which is the case for numerous elements (e.g., Fig. 4). It would further require that every U profile in every inclusion-free depth profile resulted from nearly identical core-rim curvature in every measured zircon grain. Such mixing models also exclude the resampling of previously-sampled material higher in the laser pit, which is supported by the observation that the final pits have near-vertical walls and flat bottoms (see Methods). Finally, there are several profiles in which monotonically decreasing rim-to-core U concentrations occur where Y + HREE switch from parabolic increases to decreases (Fig. 4a, c), firmly excluding mixing as a mechanism to produce the U profiles.
3. *Uranium growth zoning and/or Pb* loss* Though rare, unaltered, igneous zircon grains suggest that the protolith zircons were not zoned in U at the sub-ppm level (Fig. 4f), magmatic U zoning has been documented elsewhere (e.g., Pidgeon et al. 1998). If the U profiles were to represent relict growth zoning, any age perturbations must have resulted solely from Pb* loss, which is commonly appealed to as an age resetting mechanism. Therefore, to assess the potential significance of U growth zoning and/or Pb* diffusion on depth profile topology, we used data from the profile in Fig. 4b, which contains an apparent U diffusion profile but flat Th zoning inward of the reaction front, permitting use of the ^{208}Pb profile to assess the role of Pb* loss. Using the observed core concentrations of U and Th, we calculated U–Pb isotopic and age profiles for four scenarios, each involving igneous crystallization at 163 Ma, diffusive Pb* loss and/or U gain at the grain rim at 50 Ma, and neglecting common Pb. These models are not intended to exactly reproduce our measured depth profiles, but rather permit examination of representative concentration and age profile topologies that would result from U growth zoning and Pb* loss. Model results are shown in Fig. 11. In the case of Pb* loss without any U gain (Fig. 11a), U–Pb date topologies match the depth profiles, but Pb concentration profiles show parallel, downward-sloping arrays over the entirety of the depth profile, which is nowhere observed

in our data. In the case of a curved protolith zircon U profile coupled with Pb* loss at ~50 Ma (Fig. 11b), the modern-day ^{206}Pb and ^{207}Pb profiles are flatter, but without a Th increase, ^{208}Pb profiles show characteristic decreases with age resetting that would be resolvable outside of our method uncertainties. For example, from the core to reaction front of Fig. 4b, there is a ~40 My decrease in $^{207}\text{Pb}/^{206}\text{Pb}$ -corrected $^{206}\text{Pb}/^{238}\text{U}$ date, which—under a pure Pb* loss regime—would be associated with a ~30–40% decrease in ^{208}Pb over the same interval. In contrast, the models with only diffusive U gain (Fig. 11c) or diffusive U gain coupled with Pb* loss (Fig. 11d) produce topologies most similar to our data, including flat to increasing ^{206}Pb and ^{207}Pb and incomplete age resetting at some rims. Therefore, though we cannot rule out some contribution from Pb* loss, these models confirm that the age and U concentration data require some metamorphic U gain.

4. *Seafloor processes* Rocks and sediments exposed at the seafloor—particularly in anoxic settings—often undergo U enrichment due to redox processes (Brum-sack 2006). However, given the absence of evidence for (i) other elemental gains or losses over the same length scales as U and (ii) decrepitation of the zircon lattice, we consider such low-*T* seawater scavenging of U highly unlikely. Further, although the dates recorded by diffusively modified rims do not coalesce around a single date, they approach the metamorphic age recorded by fully recrystallized grains (below) – suggesting that the addition of U to zircon did not occur prior to eclogite-facies metamorphism. The incomplete resetting to the eclogite-facies date can be explained as a consequence of the amount of U required to fully reset magmatic zircon dates, rather than suggesting an array of older seafloor alteration dates. Because a zero-age zircon has an essentially infinite $^{238}\text{U}/^{206}\text{Pb}^*$, resetting a 163 Ma, 10-ppm U igneous grain to 60 Ma (at 50 Ma) requires the addition of ~100 ppm U; resetting it to 55 Ma requires nearly ~200 ppm U. The maximum zircon U contents measured in this study are ≤ 200 ppm, suggesting that full resetting was rarely achieved in zircon grains subject to U diffusion, and thus the youngest inner rim dates approach but may not reach the true metamorphic date.
5. *Other non-diffusive processes* Other potential explanations for the profiles could relate to fluid introduction along microcracks or nanopores, or fast diffusion through metamict zircon (e.g., Geisler et al. 2002). However, there is no CL (Fig. 2), Raman (Fig. 9), or FE-SEM evidence (Figs. S7–S8) for lattice damage, fluid inclusions, microcracks, or significant porosity, and even the most U-rich igneous zircon cores (~40 ppm) will only

become metamict on > 10 Gy timescales (Meldrum et al. 1998).

Therefore, though it is impossible to entirely rule out a non-diffusive process for U gain, we find arguments against it less viable. There are also several arguments firmly in favor of diffusive U gain, particularly that the diffusive length-scales of the U profiles are strikingly similar among different grains within the same sample and between two different samples that experienced the same metamorphic history, independent of concentration (Fig. 8)—a fundamental prediction of Fickian diffusion theory. Even under alternative diffusion scenarios not considered here—e.g., relaxation of former step function in U concentration between core and rim – the calculated diffusion coefficients would be less than an order of magnitude lower than those calculated with our fixed-boundary model, because the characteristic length-scales of required diffusion (and thus the time-integrated magnitude of diffusion, Dt) would be nearly identical. In contrast, if there was propagation of U past the deepest parts of the depth profiles (see above), the calculated diffusivities represent minima. Likewise, the relatively sharp U “peaks” in the outermost few microns of each of the U profiles are similar to natural examples attained during a changing external boundary condition (i.e., in-diffusion followed by out-diffusion; cf. Spear et al. 2012) and do not significantly alter our calculated diffusivities. Though several modeled profiles have additional, small spikes consistent with micro-inclusions or crystal defects, we emphasize that these are uncommon features (cf. Figs. S2–S3), and that such anomalies reflect the activity of a natural, stochastic diffusion process.

Finally, these rims document the “partial recrystallization” reported elsewhere in spot data (e.g., Martin et al. 2008; Chen et al. 2010; Štípská et al. 2016) in which U–Pb, trace-element, and Hf–O isotopic systematics in zircon are decoupled during metamorphism. In the Monviso samples, we are able to clarify that this decoupling involves compositional heterogeneity both ahead of and behind a reaction front, occurs over distinct length scales for different elements, and only roughly conforms to textural boundaries observed in CL.

B01 and C01: fully equilibrated metamorphic rims

The final zircon population—CL-dark metamorphic rims (Figs. 2, 10)—has the lowest REE, Th, U, and P, highest Hf, and flattest REE slopes, with highly variable Pb contents (Fig. 6). These rims are manifested texturally as oscillatory to unzoned precipitates (e.g., Fig. 2d–e), but in most grains this population is observed as a compositional endmember at the outermost rim, with apparent mixing between it and the zircon at the reaction front (e.g., Fig. 4, 10). We interpret this

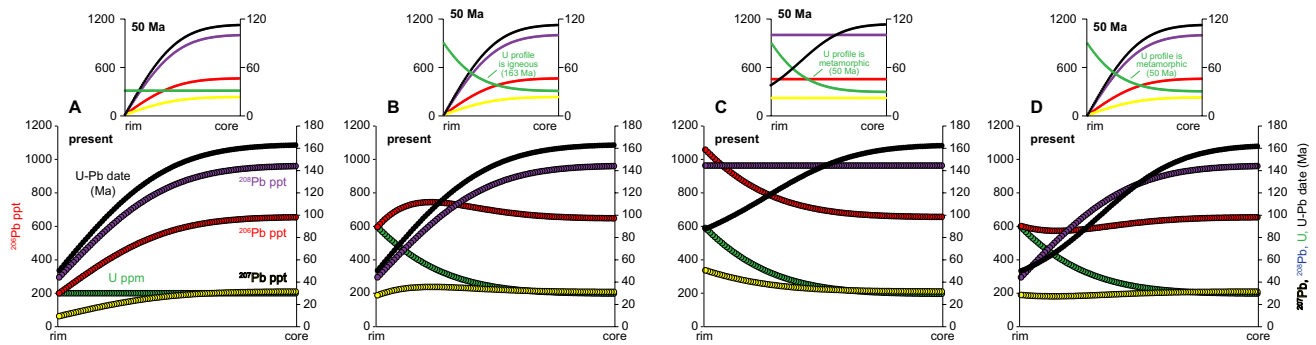


Fig. 11 Pb* loss and U gain models for age resetting in Monviso zircons. Shown are calculated modern rim-to-core profiles for U, ^{206}Pb , ^{207}Pb , ^{208}Pb , and $^{207}\text{Pb}/^{206}\text{Pb}$ -corrected $^{206}\text{Pb}/^{238}\text{U}$ age for a 163 Ma igneous zircon with 20 ppm Th that **a** experienced partial diffusive Pb* loss at 50 Ma, with no U gain; **b** experienced partial diffusive Pb* loss at 50 Ma, with an undisturbed (igneous) U profile increasing toward the rim; **c** experienced no Pb* loss, but experienced meta-

morphic U gain at 50 Ma; and **d** experienced coupled, partial diffusive Pb* loss and U gain at 50 Ma. Profiles are shown for both 50 Ma and the present. The model shows that small perturbations in U–Pb date (~10–20 My) caused by Pb* loss may not be resolvable in the depth profiling data, but that the age resetting in most grains cannot be ascribed solely to Pb* diffusion without yielding distinct Pb profile topologies

endmember as the equilibrium compositional complement to the dissolved/resorbed zircon (Fig. 2). Such replacement of trace-element rich zircon by a trace-element poor variety is commonly observed during hydrothermal alteration (Tomaschek et al. 2003; Spandler et al. 2004). New zircon precipitation did not fully balance old zircon dissolution, because many pitted and resorbed zircon surfaces lack physical rims (Fig. 2).

Precipitated zircon rim Th and U are lower than in zircon cores, but have a similar Th/U to zircon inner rims that experienced apparent U gain without Th loss (e.g., Fig. 6). In addition to the bulk depletion of REE, the relatively greater depletion of HREE suggests that precipitation occurred in the presence of metamorphic garnet, firmly tying zircon rims to eclogite-facies conditions. Many of these rims are dominated by apparent Pb decreases relative to cores, but some have Pb increases associated with more discordant isotopic data, consistent with the incorporation of Pb_C during rim precipitation. Anomalous ratios during the first few laser ablation pulses have elsewhere been attributed to incomplete laser-sample coupling, fluctuations in laser energy, or modern Pb contamination (e.g., Cottle et al. 2012; Steely et al. 2014). However, such signals persist after cleaning shots and often penetrate all the way to reaction boundaries. Further, other eclogite-facies metamorphic zircons from the same locality contain common Pb (Rubatto and Hermann 2003). Piston–cylinder experiments also suggest that common Pb is readily incorporated into zircon during hydrothermal growth (Watson et al. 1997).

For many of the depth profiles, this fully recrystallized metamorphic endmember forms an apparent mixing line with the diffusively reset inner rims (Figs. 4, 10). These mixtures may reflect analytical mixing of material from the CL-dark rims with material from the edge of CL-bright

diffusionally modified cores, especially given the patchiness of precipitated rims and the tortuosity of core–rim boundaries (Fig. 2). They may also record a geologically significant process, i.e., the progressive reaction-induced loss of trace elements (REE, U, Th, Pb, P) from grain cores as the recrystallization front progressed, and the grain rims approached their equilibrium composition with or without any new precipitation—a process that likely went to completion in rare depth profiles with entirely young dates (Fig. 4e). Finally, as noted above, they may also reflect minor out-diffusion of U. Discriminating between these processes would require higher-precision analyses of the outermost few microns of the depth profiles to better characterize their topology, e.g., by SIMS depth profiling (cf. Grove and Harrison 1999) or TEM analysis (cf. Harlov et al. 2011). Regardless of their origin, the mixing lines yield apparent isochrons with metamorphic trace-element signatures (esp. Th/U) and U–Pb dates that span between true igneous and metamorphic dates (e.g., Figs. 4a, 5). However, it is clear that any individual “isochron” date is geologically meaningless; there are no clear cut-offs in the individual depth profiles (either U–Pb date or trace-element signatures) that divide igneous crystallization from metamorphic recrystallization (Fig. 5). This is not recognizable from any one profile but requires the population-scale data to clarify. In contrast, the isolation of the most endmember, low-U rim data yields a single age population for the CL-dark rims of 51.1 ± 0.4 Ma (Fig. 7a, b), within uncertainty of the neocrystallized grains in sample M17X731A01 (Fig. 3) and consistent with the short, ≤ 1 My fluid–rock interaction timescales determined in other studies of the Monviso metaophiolite (Rubatto and Angiboust 2015; Broadwell et al. 2019). Because the diffusively reset inner rims approach this metamorphic date, we suggest that inward U diffusion was fundamentally coupled to resorption

and recrystallization. In contrast, the absence of mixing lines between the low-U, fully recrystallized rims and low-U, unaltered igneous cores (e.g., Fig. 6) shows that new zircon precipitation always occurred on previously altered grains.

Our U–Pb dates (50 ± 1 Ma [A01] and 51 ± 1 Ma [C01]) yield a significant absolute age offset from previous SHRIMP zircon U–Pb dates (45 ± 1 Ma: Rubatto and Hermann 2003; 45.8 ± 0.7 Ma: Rubatto and Angiboust 2015) for the timing of peak, eclogite-facies metamorphism at Monviso. Importantly, both methods yield internally consistent, reproducible dates, and both sets of studies date the same textural occurrence of zircon at distinct locations within the field area. Though many studies exhibit agreement between LA-ICPMS and SHRIMP U–Pb zircon dates, other studies have documented differences between these methods that may relate to matrix effects, particularly the trace-element composition of analyzed zircon (e.g., Black et al. 2004). We note that (i) the same laser-ablation methods were applied to three well-characterized secondary zircon standards during the course of this study, and each yielded a date within 0.5% of their accepted ages (see Methods), and (ii) our laser-ablation zircon dates are within uncertainty of a two-point Lu–Hf garnet-whole rock isochron date determined for a Monviso metagabbro (Duchêne et al. 1997), and further align with Ar/Ar dates from the field area (Monié and Philippot 1989). However, though our preferred interpretation is that this age difference is methodological, we cannot rule out that the discrepancy is geologic, which would require that zircon (re)crystallization at Monviso occurred over a more significant time interval (≥ 5 My) than has been previously interpreted (e.g., Rubatto and Angiboust 2015).

Low-*T* U incorporation and diffusion in zircon

Two points require resolution: first, whether the U that partitioned into resorbed zircon was internally or externally sourced, and second, why U diffusion was so rapid in the Monviso zircons.

The incorporation of U during dissolution-reprecipitation likely reflects the prevailing fluid composition, oxidation state, and mineralogy. Fluids in equilibrium with ~ 2.6 GPa, ~ 550 °C subduction-zone metabasalts are typically alkaline (several pH units above neutral: Galvez et al. 2016), which causes zircon resorption (Ayers et al. 2012). At the same time, prograde dehydration reactions experienced by the Monviso metagabbros caused the loss of oxidized rock components and a reduction in oxygen fugacity (Groppo and Castelli 2010; Angiboust et al. 2012b; Locatelli et al. 2018). Reduced U as U^{4+} is relatively insoluble in aqueous fluids (Langmuir 1978; Murphy and Shock 1999) and readily substitutes for Zr^{4+} in magmatic, metamorphic, and hydrothermal zircon (Finch and Hanchar 2003; Burnham and Berry 2012; Ayers and Peters 2018). On the other hand, U^{6+} is soluble in aqueous and especially

carbonate-bearing fluids (e.g., Murphy and Shock 1999), and there is experimental and natural evidence that magmatic zircons preferentially exclude U^{6+} (Bacon et al. 2007; Burnham and Berry 2012). Further, most minerals that contain U^{6+} do so as a uranyl ion, UO_2^{2+} (Burns et al. 1997).

To understand the oxidation state of U during eclogite-facies metamorphism of the Monviso gabbros, we calculated the relative stabilities of U complexes in aqueous fluids at 25 kbar and 550 °C (Fig. 12). Thermodynamic properties at high pressure and temperature were predicted using the Deep Earth Water model (Sverjensky et al. 2014) and the reference free energies, entropies and volumes estimated by Shock et al. (1997). The position of the quartz-fayalite-magnetite (QFM) buffer was calculated using the phase properties of Berman (1988). Species formulae follow the convention used by Shock et al. (1997) by removing H_2O molecules, e.g., UO_2 is more properly described as $U(OH)_4$ (aq). Considering the broad pH and redox constraints on eclogite-facies gabbros afforded by fluid speciation models (Galvez et al. 2016) and oxybarometry on natural rocks (Tumiati and Malaspina 2019, and references therein) (Fig. 12), U is likely to be present predominantly as U^{4+} in hydrous eclogitic fluids and thus relatively insoluble. In contrast, fluids in equilibrium with mantle serpentinite at these conditions have a similar pH (Galvez et al. 2016) but may be more oxidized (Debret and Sverjensky 2017; Iacovino et al. 2020) (although cf. Piccoli et al. 2019), which would facilitate greater U removal from the zircon reaction rim. Given the scarcity of other U-bearing phases in these rocks, the local derivation of Monviso metagabbro fluids suggested by oxygen isotope analyses (Rubatto and Angiboust 2015), and the absence of mineralogical evidence for infiltration of serpentinite-derived fluids in samples B01 and C01 (in contrast to abundant chlorite in sample A01), the most likely source of the added U was from the outer consumed zircon layer, as assumed in the moving-boundary diffusion model. In this case, U^{4+} liberated during zircon consumption accumulated at the grain boundary rather than partitioning into a reduced fluid and created a chemical potential gradient that drove diffusion ahead of the boundary (Fig. 10). We cannot rule out some U contributions from an external fluid (e.g., Angiboust et al. 2014), but they are not required. Importantly, either scenario yields the same diffusivity within uncertainty (Fig. 8). Finally, these results are consistent with U isotopic data from Izu arc volcanic rocks, which suggest that U loss from the deep mafic portions of subducting slabs is facilitated by oxidized fluid flushing from dehydrating serpentinites (Freymuth et al. 2019).

Regarding U diffusion, we note that the calculated diffusivities are remarkably faster than experimental values: D_U for the Monviso zircons is > 20 orders of magnitude higher than the parameters from high-*T* U diffusion experiments of

Cherniak et al. (1997a) extrapolated to the 550 °C metamorphic temperatures experienced by these rocks ($D_U \sim 10^{-46}$ m²/s) (Fig. 8g). They further exceed U diffusion parameters determined by Lee et al. (1997) that Cherniak et al. (1997a) argued were enhanced by recrystallization. Most strikingly, they are faster than estimated U and Th diffusion through metamict zircon at ~ 175 °C ($D_U \sim 10^{-25}$ m²/s) (Geisler et al. 2002). Even if we consider significantly longer diffusive timescales for our zircons (~ 10 My), our results only change by an order of magnitude, and still differ significantly from the extrapolated experimental data.

Ultimately, quantitative diffusion parameters depend on a significant number of factors well beyond the scope of this paper and the ability of our analytical techniques to detect (cf. Cherniak and Watson 2003; Zhang 2010; Smye et al. 2018; Dohmen et al. 2019). We can rule out some variables based on our data alone: i) there is no apparent lattice damage (Fig. 9); ii) the zircon composition does not strongly deviate from the $ZrSiO_4$ endmember and thus the role of solid solution is likely to be minimal (cf. Holder et al. 2019); and iii) there are no subgrains or major structural irregularities evident at the scale of CL analyses (Fig. 2), suggesting limited grain-boundary or pipe diffusion. Considering the confines of our data, we suggest several other possible explanations (and their limitations) for our observations:

1. A concentration-dependent diffusion mechanism (e.g., Bloch et al. 2015) is potentially viable—given the significant offset between U concentrations in this study relative to the U diffusion experiments of Cherniak et al. (1997a)—although similar effects should be observed for geochemically analogous elements with similarly low concentrations (e.g., Th). Uncommon apparent Th diffusion profiles (e.g., Fig. 4d) may suggest that Th diffusion did occur, but is less frequently observed because Th rarely partitioned back into the resorbing zircon, and thus chemical potential gradients in Th were rarer. However, a concentration-dependent mechanism is improbable because cation diffusion in zircon likely occurs by an intrinsic vacancy mechanism (Cherniak and Watson 2003).
2. Zircons exposed to high- P , silica-undersaturated solutions dissolve incongruently to produce aqueous SiO_2 and residual baddeleyite (ZrO_2) (Ayers et al. 1991). It is therefore conceivable that the zircons in this study produced a transiently porous rim in contact with a low- αSiO_2 fluid—fostering fast U in-diffusion—that later transformed to zircon as the silica activity of the fluid increased. However, there is no textural (Fig. 2, Figs. S7–S8) or Raman (Fig. 9) for relict porosity or baddeleyite, requiring complete and total back-transformation. Further, if active, this mechanism was not recorded by

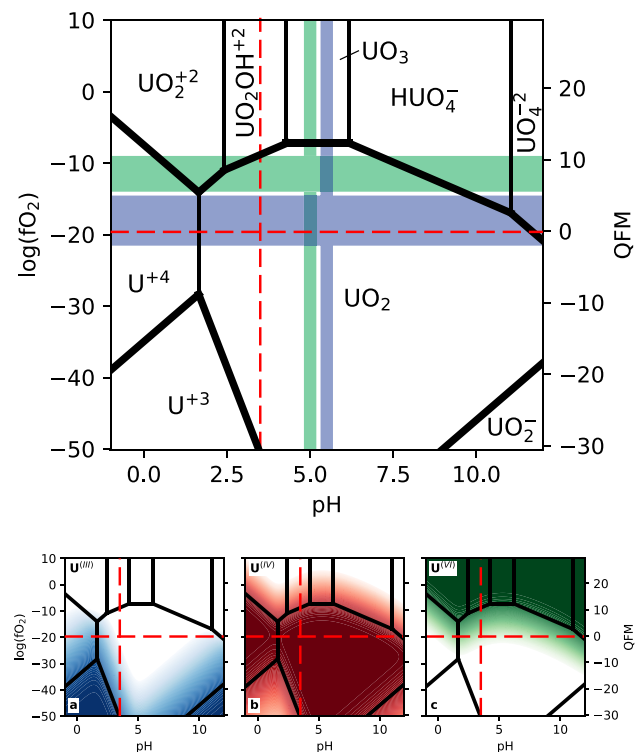


Fig. 12 Calculated U speciation in an aqueous fluid at eclogite-facies P – T conditions. Fields show the most prevalent U species in solution at 25 kbar and 550 °C, as a function of $\log(fO_2)$ and pH. Bold lines indicate changes in U oxidation state. Each panel at the bottom of the figure demonstrates the prevalence of a particular U oxidation state, as indicated in the top left corner of each panel, by the density of shading. The color scale is logarithmic and spans three orders of magnitude. Red dashed lines document neutral pH and the position of the quartz-fayalite-magnetite (QFM) buffer at the calculated P – T conditions. Subduction-zone pH and redox conditions for mafic eclogite (blue shaded regions in top panel) and serpentinite (green shaded regions in top panel) reflect both modelled (Galvez et al. 2016; Debret and Sverjensky 2017) and measured constraints (Tumiati and Malaspina 2019, and references therein)

- any other measured element, and cannot explain apparent U diffusion in advance of the defined reaction front.
3. The high fluid pressures experienced by the Monviso samples could implicate a role for H^+ solubility in the zircon lattice, which facilitates enhanced oxygen isotope diffusion in zircon (Watson and Cherniak 1997) and faster cation diffusion in mantle phases (e.g., olivine: Wang et al. 2004; ferropericlae: Demouchy et al. 2007). However, the oxygen isotopic effects occur by a mechanism distinct from cation diffusion (Watson and Cherniak 1997), and rates for wet and dry Pb diffusion in zircon have been shown to be indistinguishable within uncertainty (Cherniak and Watson 2001).
4. A final potential explanation relates to metamorphic pressure: because some cases of U–Pb and trace-element decoupling involve high- P zircons (e.g., Chen

et al. 2010; Štípská et al. 2016)—whereas U-in-zircon diffusion experiments were run at atmospheric pressure (Cherniak et al. 1997a)—our observations may relate to changes in activation volume for the experimentally measured U diffusion mechanism. However, where it has been investigated experimentally, pressure has a negligible effect on zircon cation diffusion rates (Cherniak and Watson 2001).

Without the ability to identify the atomic-scale mechanisms responsible for U diffusion during recrystallization, we can only note that this diffusion was rapid, led to significant age perturbations independent of Pb* loss (Fig. 11), occurred under fluid-saturated conditions, and is inconsistent with previous determinations of slow U diffusion in zircon. However, our results should not be interpreted as evidence for *universally* fast U diffusion in zircon; rather, our reproducible results from two distinct eclogite-facies metagabbros at Monviso suggest that such diffusion occurs in certain rocks under geologically relevant conditions, which requires further high-precision work to constrain.

Depth profiling and metamorphic zircon petrochronology

Our results show that the spatial resolution afforded by laser-ablation depth profiling can reveal endmember zircon age populations (cf. Vorhies et al. 2013; Viete et al. 2015; Lima et al. 2018; Rasmussen et al. 2019), but more importantly can also identify the geologic processes that relate them. Correct interpretation of the depth profiling data, however, requires examining individual profiles (Fig. 4) within the broad context afforded by aggregate data (Fig. 6). For example, the apparent isochrons present in most samples in this study (Fig. 5) are not meaningful, but this is not apparent by examining any single or even combination of depth profiles. Rather, the extrication of the most endmember metamorphic rims in this study yields a concise U–Pb date for fluid-rock interaction; such population identification, and avoidance of spurious U–Pb date interpretations, can be assisted in future depth-profiling studies by rigorous statistical examination of the aggregate data. We also find complex zircon compositional zoning that does not necessarily correlate with CL (e.g., the U profiles), and occurs even in regions with single age populations (e.g., Fig. 4e). This observation emphasizes that LA-ICPMS or SHRIMP spot analyses may mask age and trace-element heterogeneity not evident in CL images. If the U diffusion determined here is applicable to other zircon datasets, it would be manifested in spot data with effects similar to those inferred for Pb* loss, i.e., as a spread of concordant to discordant U–Pb isotopic data, depending on the absolute duration between crystallization and metamorphism. A final unexpected result from our study

is the recognition of “resorption ages” – those zircon rims with partially to fully reset U–Pb dates driven solely by U in-diffusion. Regardless of whether or not zircon rim resetting is caused by Pb* or U mobility, pooling of depth profiling analyses on altered or partially resorbed zircon may, therefore, allow recognition of lower-*T* fluid rock interaction, even where new zircon metamorphic rims are not present.

Conclusions

1. Zircons from eclogite-facies Monviso metagabbros experienced a spectrum of responses to metamorphism, including diffusional modification of igneous cores, dissolution-precipitation recrystallization, and in one sample, new grain growth. For partially recrystallized grains that exhibit complex age spectra, we discriminate three endmember populations that exhibit a series of two-component mixing arrays – indicating that resorption, recrystallization, and diffusion were fundamentally coupled. These mixing arrays form apparent isochrons, but yield erroneous dates.
2. Length-scales of dissolution-precipitation recrystallization are typically short ($\leq 5 \mu\text{m}$), but apparent diffusional length-scales for U are up to $\sim 15 \mu\text{m}$. The continuous range of ages observed in the dataset is ascribed primarily to U mobility in otherwise unaltered zircon, although we cannot rule out some Pb* loss.
3. The inward diffusion of U into zircon cores decoupled U–Pb and trace-element systematics in zircon rims. However, dates from the most recrystallized zircon suggest short-duration fluid-rock interaction at peak metamorphic conditions, consistent with previous studies.
4. Calculated U diffusion parameters for the Monviso zircons are significantly faster than predicted experimentally, suggesting a diffusion mechanism distinct from that measured experimentally. There is some evidence for Th diffusion at the same conditions, but P, REE, and Pb were effectively immobile throughout recrystallization. Our data therefore record a previously unrecognized age resetting process in metamorphic zircon.

Acknowledgements We thank P. Starr for sharing field notes and sample context, H. Marschall for access to the SelFrag, J. Cottle for error propagation advice, J. Singer for CL expertise, and M. Wetherington for Raman assistance. We also acknowledge the ExTerra Field Institute and Research Endeavor (E-FIRE) program participants, including field assistance from P. Agard, M. Locatelli, and S. Angiboust. We are grateful to D. Rubatto, E. B. Watson, and two anonymous reviewers for comments that significantly improved the manuscript, and to D. Rubatto for editorial handling. This work was funded by National Science Foundation Grant OISE-1545903.

References

- Agard P, Jolivet L, Goffe B (2001) Tectonometamorphic evolution of the Schistes Lustrés Complex; implications for the exhumation of HP and UHP rocks in the Western Alps. *Bulletin Soc Géol Fr* 172(5):617–636. <https://doi.org/10.2113/172.5.617>
- Agard P, Yamato P, Jolivet L, Burov E (2009) Exhumation of oceanic blueschists and eclogites in subduction zones: Timing and mechanisms. *Earth Sci Rev* 92(1):53–79. <https://doi.org/10.1016/j.earscirev.2008.11.002>
- Angiboust S, Agard P, Jolivet L, Beyssac O (2009) The Zermatt-Saas ophiolite: the largest (60-km wide) and deepest (c. 70–80 km) continuous slice of oceanic lithosphere detached from a subduction zone? *Terra Nova* 21(3):171–180. <https://doi.org/10.1111/j.1365-3121.2009.00870.x>
- Angiboust S, Agard P, Raimbourg H, Yamato P, Huet B (2011) Subduction interface processes recorded by eclogite-facies shear zones (Monviso, W. Alps). *Lithos* 127(1):222–238. <https://doi.org/10.1016/j.lithos.2011.09.004>
- Angiboust S, Agard P, Yamato P, Raimbourg H (2012a) Eclogite breccias in a subducted ophiolite: A record of intermediate-depth earthquakes? *Geology* 40(8):707–710. <https://doi.org/10.1130/g32925.1>
- Angiboust S, Langdon R, Agard P, Waters D, Chopin C (2012b) Eclogitization of the Monviso ophiolite (W. Alps) and implications on subduction dynamics. *J Metamorph Geol* 30(1):37–61. <https://doi.org/10.1111/j.1525-1314.2011.00951.x>
- Angiboust S, Pettko T, De Hoog JCM, Caron B, Oncken O (2014) Channelized fluid flow and eclogite-facies metasomatism along the subduction shear zone. *J Pet* 55(5):883–916. <https://doi.org/10.1093/petrology/egu010>
- Ayers JC, Peters TJ (2018) Zircon/fluid trace element partition coefficients measured by recrystallization of Mud Tank zircon at 1.5 GPa and 800–1000 °C. *Geochim Cosmochim Acta* 223:60–74. <https://doi.org/10.1016/j.gca.2017.11.025>
- Ayers JC, Watson EB, Tarney J, Pickering KT, Knipe RJ, Dewey John F (1991) Solubility of apatite, monazite, zircon, and rutile in supercritical aqueous fluids with implications for subduction zone geochemistry. *Philos Trans R Soc Lond Ser A Phys Eng Sci* 335(1638):365–375. <https://doi.org/10.1098/rsta.1991.0052>
- Ayers JC, Zhang L, Luo Y, Peters TJ (2012) Zircon solubility in alkaline aqueous fluids at upper crustal conditions. *Geochim Cosmochim Acta* 96:18–28. <https://doi.org/10.1016/j.gca.2012.08.027>
- Bacon CR, Sisson TW, Mazdab FK (2007) Young cumulate complex beneath Veniaminof caldera, Aleutian arc, dated by zircon in erupted plutonic blocks. *Geology* 35(6):491–494. <https://doi.org/10.1130/g23446a.1>
- Belousova E, Griffin W, O'Reilly SY, Fisher N (2002) Igneous zircon: trace element composition as an indicator of source rock type. *Contrib Miner Pet* 143(5):602–622. <https://doi.org/10.1007/s00410-002-0364-7>
- Beltrando M, Compagnoni R, Lombardo B (2010) (Ultra-) High-pressure metamorphism and orogenesis: an Alpine perspective. *Gondwana Res* 18(1):147–166. <https://doi.org/10.1016/j.gr.2010.01.009>
- Berman RG (1988) Internally-Consistent Thermodynamic Data for Minerals in the System Na₂O-K₂O-CaO-MgO-FeO-Fe₂O₃-Al₂O₃-SiO₂-TiO₂-H₂O-CO₂. *J Petrol* 29(2):445–522. <https://doi.org/10.1093/petrology/29.2.445>
- Black LP, Kamo SL, Allen CM, Davis DW, Aleinikoff JN, Valley JW, Mundil R, Campbell IH, Korsch RJ, Williams IS, Foudoulis C (2004) Improved ²⁰⁶Pb/²³⁸U microprobe geochronology by the monitoring of a trace-element-related matrix effect; SHRIMP, ID-TIMS, ELA-ICP-MS and oxygen isotope documentation for a series of zircon standards. *Chem Geol* 205(1):115–140. <https://doi.org/10.1016/j.chemgeo.2004.01.003>
- Bloch E, Ganguly J, Hervig R, Cheng W (2015) ¹⁷⁶Lu–¹⁷⁶Hf geochronology of garnet I: experimental determination of the diffusion kinetics of Lu³⁺ and Hf⁴⁺ in garnet, closure temperatures and geochronological implications. *Contrib Miner Pet* 169(2):12. <https://doi.org/10.1007/s00410-015-1109-8>
- Broadwell KS, Locatelli M, Verlaquet A, Agard P, Caddick MJ (2019) Transient and periodic brittle deformation of eclogites during intermediate-depth subduction. *Earth Planet Sci Lett* 521:91–102. <https://doi.org/10.1016/j.epsl.2019.06.008>
- Brumsack H-J (2006) The trace metal content of recent organic carbon-rich sediments: Implications for Cretaceous black shale formation. *Palaeogeogr Palaeoclimatol Palaeoecol* 232(2–4):344–361. <https://doi.org/10.1016/j.palaeo.2005.05.011>
- Burnham AD, Berry AJ (2012) An experimental study of trace element partitioning between zircon and melt as a function of oxygen fugacity. *Geochim Cosmochim Acta* 95:196–212. <https://doi.org/10.1016/j.gca.2012.07.034>
- Burns PC, Ewing RC, Hawthorne FC (1997) The crystal chemistry of hexavalent uranium; polyhedron geometries, bond-valence parameters, and polymerization of polyhedra. *Can Mineralog* 35(6):1551–1570
- Carlson WD (2012) Rates and mechanism of Y, REE, and Cr diffusion in garnet. *Am Miner* 97(10):1598–1618. <https://doi.org/10.2138/am.2012.4108>
- Chen R-X, Zheng Y-F, Xie L (2010) Metamorphic growth and recrystallization of zircon: Distinction by simultaneous in-situ analyses of trace elements, U-Th-Pb and Lu-Hf isotopes in zircons from eclogite-facies rocks in the Sulu orogen. *Lithos* 114(1–2):132–154. <https://doi.org/10.1016/j.lithos.2009.08.006>
- Cherniak DJ, Hanchar JM, Watson EB (1997a) Diffusion of tetravalent cations in zircon. *Contrib Miner Pet* 127(4):383–390. <https://doi.org/10.1007/s004100050287>
- Cherniak DJ, Hanchar JM, Watson EB (1997b) Rare-earth diffusion in zircon. *Chem Geol* 134(4):289–301. [https://doi.org/10.1016/S0009-2541\(96\)00098-8](https://doi.org/10.1016/S0009-2541(96)00098-8)
- Cherniak DJ, Lanford WA, Ryerson FJ (1991) Lead diffusion in apatite and zircon using ion implantation and Rutherford Backscattering techniques. *Geochim Cosmochim Acta* 55(6):1663–1673. [https://doi.org/10.1016/0016-7037\(91\)90137-T](https://doi.org/10.1016/0016-7037(91)90137-T)
- Cherniak DJ, Watson EB (2001) Pb diffusion in zircon. *Chem Geol* 172(1):5–24. [https://doi.org/10.1016/S0009-2541\(00\)00233-3](https://doi.org/10.1016/S0009-2541(00)00233-3)
- Cherniak DJ, Watson EB (2003) Diffusion in zircon. *Rev Mineral Geochem* 53(1):113–143. <https://doi.org/10.2113/0530113>
- Cliff RA, Barnicoat AC, Inger S (1998) Early tertiary eclogite facies metamorphism in the monviso ophiolite. *J Metamorph Geol* 16(3):447–455. <https://doi.org/10.1111/j.1525-1314.1998.00147.x>
- Cottle JM, Horstwood MSA, Parrish RR (2009) A new approach to single shot laser ablation analysis and its application to in situ Pb/U geochronology. *J Anal At Spectrom* 24(10):1355–1363. <https://doi.org/10.1039/B821899D>
- Cottle JM, Kylander-Clark AR, Vrijmoed JC (2012) U-Th/Pb geochronology of detrital zircon and monazite by single shot laser ablation inductively coupled plasma mass spectrometry (SS-LA-ICPMS). *Chem Geol* 332–333:136–147. <https://doi.org/10.1016/j.chemgeo.2012.09.035>
- Coward M, Dietrich D (1989) Alpine tectonics—an overview. *Geol Soc Lond, Sp Publ* 45(1):1–29. <https://doi.org/10.1144/gsl.sp.1989.045.01.01>
- Crank J (1975) *The mathematics of diffusion*. Brunel University Press, Uxbridge
- Debret B, Sverjensky DA (2017) Highly oxidising fluids generated during serpentinite breakdown in subduction zones. *Sci Rep* 7(1):10351. <https://doi.org/10.1038/s41598-017-09626-y>

- Demouchy S, Mackwell SJ, Kohlstedt DL (2007) Influence of hydrogen on Fe–Mg interdiffusion in (Mg, Fe)O and implications for Earth's lower mantle. *Contrib Miner Pet* 154(3):279–289. <https://doi.org/10.1007/s00410-007-0193-9>
- Dickinson WR, Gehrels GE (2003) U–Pb ages of detrital zircons from Permian and Jurassic eolian sandstones of the Colorado Plateau, USA: paleogeographic implications. *Sed Geol* 163(1):29–66. [https://doi.org/10.1016/S0037-0738\(03\)00158-1](https://doi.org/10.1016/S0037-0738(03)00158-1)
- Dohmen R, Marschall HR, Ludwig T, Polednia J (2019) Diffusion of Zr, Hf, Nb and Ta in rutile: effects of temperature, oxygen fugacity, and doping level, and relation to rutile point defect chemistry. *Phys Chem Miner* 46(3):311–332. <https://doi.org/10.1007/s00269-018-1005-7>
- Duchêne S, Blichert-Toft J, Luais B, Télouk P, Lardeaux JM, Albarède F (1997) The Lu–Hf dating of garnets and the ages of the Alpine high-pressure metamorphism. *Nature* 387(6633):586–589. <https://doi.org/10.1038/42446>
- Finch RJ, Hanchar JM (2003) Structure and chemistry of zircon and zircon-group minerals. *Rev Mineral Geochem* 53(1):1–25. <https://doi.org/10.2113/0530001>
- Freyruth H, Andersen MB, Elliott T (2019) Uranium isotope fractionation during slab dehydration beneath the Izu arc. *Earth Planet Sci Lett* 522:244–254. <https://doi.org/10.1016/j.epsl.2019.07.006>
- Galvez ME, Connolly JAD, Manning CE (2016) Implications for metal and volatile cycles from the pH of subduction zone fluids. *Nature* 539:420. <https://doi.org/10.1038/nature20103>
- Gauthiez-Putallaz L, Rubatto D, Hermann J (2016) Dating prograde fluid pulses during subduction by in situ U–Pb and oxygen isotope analysis. *Contrib Miner Pet* 171(2):15. <https://doi.org/10.1007/s00410-015-1226-4>
- Geisler T, Pidgeon RT, Kurtz R, van Bronswijk W, Schleicher H (2003a) Experimental hydrothermal alteration of partially metamict zircon. *Am Miner* 88(10):1496–1513. <https://doi.org/10.2138/am-2003-1013>
- Geisler T, Pidgeon RT, van Bronswijk W, Kurtz R (2002) Transport of uranium, thorium, and lead in metamict zircon under low-temperature hydrothermal conditions. *Chem Geol* 191(1):141–154. [https://doi.org/10.1016/S0009-2541\(02\)00153-5](https://doi.org/10.1016/S0009-2541(02)00153-5)
- Geisler T, Rashwan AA, Rahn MKW, Poller U, Zwingmann H, Pidgeon RT, Schleicher H, Tomaschek F (2003b) Low-temperature hydrothermal alteration of natural metamict zircons from the Eastern Desert, Egypt. *Mineral Mag* 67(3):485–508. <https://doi.org/10.1180/0026461036730112>
- Geisler T, Schaltegger U, Tomaschek F (2007) Re-equilibration of Zircon in Aqueous Fluids and Melts. *Elements* 3(1):43–50. <https://doi.org/10.2113/gselements.3.1.43>
- Groppo C, Castelli D (2010) Prograde P–T evolution of a lawsonite eclogite from the monviso meta-ophiolite (Western Alps): dehydration and redox reactions during subduction of oceanic FeTi-oxide gabbro. *J Pet* 51(12):2489–2514. <https://doi.org/10.1093/ptrology/egq065>
- Grove M, Harrison TM (1999) Monazite Th–Pb age depth profiling. *Geology* 27(6):487–490. [https://doi.org/10.1130/0091-7613\(1999\)027%3c0487:mtpadp%3e2.3.co;2](https://doi.org/10.1130/0091-7613(1999)027%3c0487:mtpadp%3e2.3.co;2)
- Harley SL, Kelly NM, Möller A (2007) Zircon behaviour and the thermal histories of mountain chains. *Elements* 3(1):25–30. <https://doi.org/10.2113/gselements.3.1.25>
- Harlow DE, Wirth R, Hetherington CJ (2011) Fluid-mediated partial alteration in monazite: the role of coupled dissolution–reprecipitation in element redistribution and mass transfer. *Contrib Miner Pet* 162(2):329–348. <https://doi.org/10.1007/s00410-010-0599-7>
- Hesse MA (2012) A finite volume method for trace element diffusion and partitioning during crystal growth. *Comput Geosci* 46:96–106. <https://doi.org/10.1016/j.cageo.2012.04.009>
- Hiess J, Condon DJ, McLean N, Noble SR (2012) $^{238}\text{U}/^{235}\text{U}$ systematics in terrestrial uranium-bearing minerals. *Science* 335(6076):1610–1614
- Holder RM, Hacker BR, Seward GGE, Kylander-Clark ARC (2019) Interpreting titanite U–Pb dates and Zr thermobarometry in high-grade rocks: empirical constraints on elemental diffusivities of Pb, Al, Fe, Zr, Nb, and Ce. *Contrib Miner Pet* 174(5):42. <https://doi.org/10.1007/s00410-019-1578-2>
- Iacovino K, Guild MR, Till CB (2020) Aqueous fluids are effective oxidizing agents of the mantle in subduction zones. *Contrib Miner Petrol* 175(4):36. <https://doi.org/10.1007/s00410-020-1673-4>
- Jackson SE, Pearson NJ, Griffin WL, Belousova EA (2004) The application of laser ablation-inductively coupled plasma-mass spectrometry to in situ U–Pb zircon geochronology. *Chem Geol* 211(1):47–69. <https://doi.org/10.1016/j.chemgeo.2004.06.017>
- Kolesov BA, Geiger CA, Armbruster T (2001) The dynamic properties of zircon studied by single-crystal X-ray diffraction and Raman spectroscopy. *Eur J Mineral* 13(5):939–948. <https://doi.org/10.1127/0935-1221/2001/0013-0939>
- Kusiak MA, Dunkley DJ, Wirth R, Whitehouse MJ, Wilde SA, Marquardt K (2015) Metallic lead nanospheres discovered in ancient zircons. *Proc Natl Acad Sci USA* 112(16):4958–4963. <https://doi.org/10.1073/pnas.1415264112>
- Kusiak MA, Whitehouse MJ, Wilde SA, Nemchin AA, Clark C (2013) Mobilization of radiogenic Pb in zircon revealed by ion imaging: Implications for early Earth geochronology. *Geology* 41(3):291–294. <https://doi.org/10.1130/g33920.1>
- Kylander-Clark ARC, Hacker BR, Cottle JM (2013) Laser-ablation split-stream ICP petrochronology. *Chem Geol* 345:99–112. <https://doi.org/10.1016/j.chemgeo.2013.02.019>
- Lagabrielle Y, Cannat M (1990) Alpine Jurassic ophiolites resemble the modern central Atlantic basement. *Geology* 18(4):319–322. [https://doi.org/10.1130/0091-7613\(1990\)018%3c0319:ajortm%3e2.3.co;2](https://doi.org/10.1130/0091-7613(1990)018%3c0319:ajortm%3e2.3.co;2)
- Lagabrielle Y, Lemoine M (1997) Alpine, Corsican and Apennine ophiolites: the slow-spreading ridge model. *Comptes Rendus de l'Académie des Sci Ser IIA Earth Planet Sci* 325(12):909–920. [https://doi.org/10.1016/S1251-8050\(97\)82369-5](https://doi.org/10.1016/S1251-8050(97)82369-5)
- Lagabrielle Y, Vitale Brovarone A, Ildefonso B (2015) Fossil oceanic core complexes recognized in the blueschist metaophiolites of Western Alps and Corsica. *Earth Sci Rev* 141:1–26. <https://doi.org/10.1016/j.earscirev.2014.11.004>
- Langmuir D (1978) Uranium solution-mineral equilibria at low temperatures with applications to sedimentary ore deposits. *Geochimica Cosmochimica Acta* 42(6):547–569. [https://doi.org/10.1016/0016-7037\(78\)90001-7](https://doi.org/10.1016/0016-7037(78)90001-7)
- Lee JKW, Williams IS, Ellis DJ (1997) Pb, U and Th diffusion in natural zircon. *Nature* 390(6656):159–162. <https://doi.org/10.1038/36554>
- Li X-H, Faure M, Rossi P, Lin W, Lahondère D (2015) Age of Alpine Corsica ophiolites revisited: Insights from in situ zircon U–Pb age and O–Hf isotopes. *Lithos* 220–223:179–190. <https://doi.org/10.1016/j.lithos.2015.02.006>
- Lima RD, Prior MG, Stockli DF, Hayman NW (2018) Protracted heating of the orogenic crust in Death Valley, California, USA. *Geology* 46(4):315–318. <https://doi.org/10.1130/g39865.1>
- Locatelli M, Verlaquet A, Agard P, Federico L, Angiboust S (2018) Intermediate-depth brecciation along the subduction plate interface (Monviso eclogite, W. Alps). *Lithos* 320–321:378–402. <https://doi.org/10.1016/j.lithos.2018.09.028>
- Lombardo B, Nervo R, Compagnoni R, Messiga B, Kienast JR, Mevel C, Fiora L, Piccardo GB, Lanza R (1978) Osservazioni preliminari sulle ofioliti metamorfiche del Monviso (Alpi occidentali). *Rendiconti Soc It Mineral Pet* 34:253–305

- Ludwig KR (2003) Isoplot 3.00: a geochronological toolkit for microsoft excel. Berkeley Geochronology Center Special Publication, Berkeley, USA
- Manatschal G, Müntener O (2009) A type sequence across an ancient magma-poor ocean–continent transition: the example of the western Alpine Tethys ophiolites. *Tectonophysics* 473(1):4–19. <https://doi.org/10.1016/j.tecto.2008.07.021>
- Martin LAJ, Duchêne S, Deloule E, Vanderhaeghe O (2008) Mobility of trace elements and oxygen in zircon during metamorphism: Consequences for geochemical tracing. *Earth Planet Sci Lett* 267(1):161–174. <https://doi.org/10.1016/j.epsl.2007.11.029>
- Meldrum A, Boatner LA, Weber WJ, Ewing RC (1998) Radiation damage in zircon and monazite. *Geochim Cosmochim Acta* 62(14):2509–2520. [https://doi.org/10.1016/S0016-7037\(98\)00174-4](https://doi.org/10.1016/S0016-7037(98)00174-4)
- Monié P, Philippot P (1989) Mise en évidence de l'âge Eocene Moyen du métamorphisme de haute-pression dans la nappe ophiolitique du Monviso (Alpes Occidentales) par la méthode ^{40}Ar - ^{39}Ar . *Comptes Rendus de l'Académie des Sciences, Paris Ser* 2(309):245–251
- Murphy WM, Shock EL (1999) Environmental aqueous geochemistry of actinides. In: Burns PC, Finch RJ (eds) Uranium: mineralogy, geochemistry, and the environment, vol 38. Mineralogical Society of America, Chantilly, USA, p 679
- Nasdala L, Irmer G, Wolf D (1995) The degree of metamictization in zircon; a Raman spectroscopic study. *Eur J Mineral* 7(3):471–478
- Paton C, Hellstrom J, Paul B, Woodhead J, Hergt J (2011) Iolite: freeware for the visualisation and processing of mass spectrometric data. *J Anal At Spectrom* 26(12):2508–2518. <https://doi.org/10.1039/C1JA10172B>
- Peterman EM, Reddy SM, Saxey DW, Snoeyenbos DR, Rickard WDA, Fougereuse D, Kylander-Clark ARC (2016) Nanogeochronology of discordant zircon measured by atom probe microscopy of Pb-enriched dislocation loops. *Sci Adv* 2(9):e1601318. <https://doi.org/10.1126/sciadv.1601318>
- Philippot P, Kienast J-R (1989) Chemical-microstructural changes in eclogite-facies shear zones (Monviso, Western Alps, north Italy) as indicators of strain history and the mechanism and scale of mass transfer. *Lithos* 23(3):179–200. [https://doi.org/10.1016/0024-4937\(89\)90004-2](https://doi.org/10.1016/0024-4937(89)90004-2)
- Philippot P, Selverstone J (1991) Trace-element-rich brines in eclogitic veins: implications for fluid composition and transport during subduction. *Contrib Miner Petrol* 106(4):417–430. <https://doi.org/10.1007/BF00321985>
- Piccoli F, Hermann J, Petke T, Connolly JAD, Kempf ED, Vieira Duarte JF (2019) Subducting serpentinites release reduced, not oxidized, aqueous fluids. *Sci Rep* 9(1):19573. <https://doi.org/10.1038/s41598-019-55944-8>
- Pidgeon RT (1992) Recrystallisation of oscillatory zoned zircon: some geochronological and petrological implications. *Contrib Miner Pet* 110(4):463–472. <https://doi.org/10.1007/BF00344081>
- Pidgeon RT (2014) Zircon radiation damage ages. *Chem Geol* 367:13–22. <https://doi.org/10.1016/j.chemgeo.2013.12.010>
- Pidgeon RT, Nemchin AA, Hitchen GJ (1998) Internal structures of zircons from Archaean granites from the Darling Range batholith: implications for zircon stability and the interpretation of zircon U-Pb ages. *Contrib Miner Petrol* 132(3):288–299. <https://doi.org/10.1007/s004100050422>
- Putnis A (2009) Mineral replacement reactions. *Rev Miner Geochem* 70(1):87–124. <https://doi.org/10.2138/rmg.2009.70.3>
- Putnis CV, Tsukamoto K, Nishimura Y (2005) Direct observations of pseudomorphism: compositional and textural evolution at a fluid-solid interface. *Am Miner* 90(11–12):1909–1912. <https://doi.org/10.2138/am.2005.1990>
- Rasmussen C, Stockli DF, Ross CH, Pickersgill A, Gulick SP, Schmieder M, Christeson GL, Wittmann A, Kring DA, Morgan JV (2019) U-Pb memory behavior in Chicxulub's peak ring—applying U-Pb depth profiling to shocked zircon. *Chem Geol* 525:356–367. <https://doi.org/10.1016/j.chemgeo.2019.07.029>
- Rioux M, Jöns N, Bowring S, Lissenberg CJ, Bach W, Kylander-Clark A, Hacker B, Dudás F (2014IB) U-Pb dating of interspersed gabbroic magmatism and hydrothermal metamorphism during lower crustal accretion, Vema lithospheric section, Mid-Atlantic Ridge. *J Geophys Res Solid Earth* 120(4):2014B01168. <https://doi.org/10.1002/2014JB011668>
- Rubatto D (2017) Zircon: the metamorphic mineral. *Rev Miner Geochem* 83(1):261–295. <https://doi.org/10.2138/rmg.2017.83.9>
- Rubatto D, Angiboust S (2015) Oxygen isotope record of oceanic and high-pressure metasomatism: a P-T-time–fluid path for the Monviso eclogites (Italy). *Contrib Miner Petrol* 170(5):44. <https://doi.org/10.1007/s00410-015-1198-4>
- Rubatto D, Gebauer D (2000) Use of cathodoluminescence for U-Pb zircon dating by ion microprobe: some examples from the Western Alps. In: Pagel M, Barbin V, Blanc P, Ohnenstetter D (eds) Cathodoluminescence in geosciences. Springer, Berlin, Heidelberg, Berlin, pp 373–400
- Rubatto D, Hermann J (2003) Zircon formation during fluid circulation in eclogites (Monviso, Western Alps): implications for Zr and Hf budget in subduction zones. *Geochim Cosmochim Acta* 67(12):2173–2187. [https://doi.org/10.1016/S0016-7037\(02\)01321-2](https://doi.org/10.1016/S0016-7037(02)01321-2)
- Rubatto D, Hermann J (2007) Experimental zircon/melt and zircon/garnet trace element partitioning and implications for the geochronology of crustal rocks. *Chem Geol* 241(1–2):38–61. <https://doi.org/10.1016/j.chemgeo.2007.01.027>
- Rubatto D, Regis D, Hermann J, Boston K, Engi M, Beltrando M, McAlpine SRB (2011) Yo-yo subduction recorded by accessory minerals in the Italian Western Alps. *Nat Geosci* 4:338. <https://doi.org/10.1038/ngeo1124>
- Schmidt C, Steele-MacInnis M, Watenphul A, Wilke M (2013) Calibration of zircon as a Raman spectroscopic pressure sensor to high temperatures and application to water-silicate melt systems. *Am Miner* 98(4):643–650. <https://doi.org/10.2138/am.2013.4143>
- Seydoux-Guillaume A-M, Bingen B, Paquette J-L, Bosse V (2015) Nanoscale evidence for uranium mobility in zircon and the discordance of U-Pb chronometers. *Earth Planet Sci Lett* 409:43–48. <https://doi.org/10.1016/j.epsl.2014.10.044>
- Shock EL, Sassani DC, Betz H (1997) Uranium in geologic fluids: Estimates of standard partial molal properties, oxidation potentials, and hydrolysis constants at high temperatures and pressures. *Geochim Cosmochim Acta* 61(20):4245–4266. [https://doi.org/10.1016/S0016-7037\(97\)00240-8](https://doi.org/10.1016/S0016-7037(97)00240-8)
- Sláma J, Košler J, Condon DJ, Crowley JL, Gerdes A, Hancher JM, Horstwood MSA, Morris GA, Nasdala L, Norberg N, Schaltegger U, Schoene B, Tubrett MN, Whitehouse MJ (2008) Plešovice zircon—a new natural reference material for U-Pb and Hf isotopic microanalysis. *Chem Geol* 249(1):1–35. <https://doi.org/10.1016/j.chemgeo.2007.11.005>
- Smye AJ, Jackson CRM, Konrad-Schmolke M, Hesse MA, Parman SW, Shuster DL, Ballentine CJ (2017) Noble gases recycled into the mantle through cold subduction zones. *Earth Planet Sci Lett* 471:65–73. <https://doi.org/10.1016/j.epsl.2017.04.046>
- Smye AJ, Marsh JH, Vermeesch P, Garber JM, Stockli DF (2018) Applications and limitations of U-Pb thermochronology to middle and lower crustal thermal histories. *Chem Geol* 494:1–18. <https://doi.org/10.1016/j.chemgeo.2018.07.003>
- Smye AJ, Stockli DF (2014) Rutile U-Pb age depth profiling: a continuous record of lithospheric thermal evolution. *Earth Planet Sci Lett* 408:171–182. <https://doi.org/10.1016/j.epsl.2014.10.013>

- Soman A, Geisler T, Tomaschek F, Grange M, Berndt J (2010) Alteration of crystalline zircon solid solutions: a case study on zircon from an alkaline pegmatite from Zomba-Malosa, Malawi. *Contrib Mineral Pet* 160(6):909–930. <https://doi.org/10.1007/s00410-010-0514-2>
- Spandler C, Hermann J, Rubatto D (2004) Exsolution of thortveitite, yttrialite, and xenotime during low-temperature recrystallization of zircon from New Caledonia, and their significance for trace element incorporation in zircon. *Am Mineral* 89(11–12):1795. <https://doi.org/10.2138/am-2004-11-1226>
- Spandler C, Pettke T, Rubatto D (2011) Internal and external fluid sources for eclogite-facies veins in the monviso meta-ophiolite, Western Alps: implications for fluid flow in subduction zones. *J Pet* 52(6):1207–1236. <https://doi.org/10.1093/ptrology/egr025>
- Spear FS, Ashley KT, Webb LE, Thomas JB (2012) Ti diffusion in quartz inclusions: implications for metamorphic time scales. *Contrib Miner Pet* 164(6):977–986. <https://doi.org/10.1007/s00410-012-0783-z>
- Stacey JS, Kramers JD (1975) Approximation of terrestrial lead isotope evolution by a two-stage model. *Earth Planet Sci Lett* 26(2):207–221. [https://doi.org/10.1016/0012-821X\(75\)90088-6](https://doi.org/10.1016/0012-821X(75)90088-6)
- Stearns MA, Cottle JM, Hacker BR, Kylander-Clark ARC (2016) Extracting thermal histories from the near-rim zoning in titanite using coupled U-Pb and trace-element depth profiles by single-shot laser-ablation split stream (SS-LASS) ICP-MS. *Chem Geol* 422:13–24. <https://doi.org/10.1016/j.chemgeo.2015.12.011>
- Steely AN, Hourigan JK, Juel E (2014) Discrete multi-pulse laser ablation depth profiling with a single-collector ICP-MS: Sub-micron U-Pb geochronology of zircon and the effect of radiation damage on depth-dependent fractionation. *Chem Geol* 372:92–108. <https://doi.org/10.1016/j.chemgeo.2014.02.021>
- Štípská P, Powell R, Hacker BR, Holder R, Kylander-Clark ARC (2016) Uncoupled U/Pb and REE response in zircon during the transformation of eclogite to mafic and intermediate granulite (Blanský les, Bohemian Massif). *J Metamorph Geol* 34(6):551–572. <https://doi.org/10.1111/jmg.12193>
- Sverjensky DA, Harrison B, Azzolini D (2014) Water in the deep Earth: the dielectric constant and the solubilities of quartz and corundum to 60 kb and 1200°C. *Geochim Cosmochim Acta* 129:125–145. <https://doi.org/10.1016/j.gca.2013.12.019>
- Taylor RJM, Clark C, Harley SL, Kylander-Clark ARC, Hacker BR, Kinny PD (2017) Interpreting granulite facies events through rare earth element partitioning arrays. *J Metamorph Geol* 35(7):759–775. <https://doi.org/10.1111/jmg.12254>
- Tomaschek F, Kennedy AK, Villa IM, Lagos M, Ballhaus C (2003) Zircons from Syros, Cyclades, Greece—recrystallization and mobilization of zircon during high-pressure metamorphism. *J Pet* 44(11):1977–2002. <https://doi.org/10.1093/ptrology/egg067>
- Tumiati S, Malaspina N (2019) Redox processes and the role of carbon-bearing volatiles from the slab–mantle interface to the mantle wedge. *J Geol Soc* 176(2):388–397. <https://doi.org/10.1144/jgs2018-046>
- Valley JW, Cavosie AJ, Ushikubo T, Reinhard DA, Lawrence DF, Larson DJ, Clifton PH, Kelly TF, Wilde SA, Moser DE, Spicuzza MJ (2014) Hadean age for a post-magma-ocean zircon confirmed by atom-probe tomography. *Nat Geosci* 7:219. <https://doi.org/10.1038/ngeo2075>
- Vavra G, Schmid R, Gebauer D (1999) Internal morphology, habit and U-Th-Pb microanalysis of amphibolite-to-granulite facies zircons: geochronology of the Ivrea Zone (Southern Alps). *Contrib Miner Petrol* 134(4):380–404. <https://doi.org/10.1007/s004100050492>
- Viete DR, Kylander-Clark ARC, Hacker BR (2015) Single-shot laser ablation split stream (SS-LASS) petrochronology deciphers multiple, short-duration metamorphic events. *Chem Geol* 415:70–86. <https://doi.org/10.1016/j.chemgeo.2015.09.013>
- Vitale Brovarone A, Beltrando M, Malavieille J, Giuntoli F, Tondella E, Groppo C, Beyssac O, Compagnoni R (2011) Inherited ocean-continent transition zones in deeply subducted terranes: insights from Alpine Corsica. *Lithos* 124(3):273–290. <https://doi.org/10.1016/j.lithos.2011.02.013>
- Vorhies SH, Ague JJ, Schmitt AK (2013) Zircon growth and recrystallization during progressive metamorphism, Barrovian zones, Scotland. *Am Mineralog* 98(1):219–230. <https://doi.org/10.2138/am.2013.4240>
- Wang Z, Hiraga T, Kohlstedt DL (2004) Effect of H⁺ on Fe–Mg interdiffusion in olivine, (Fe, Mg)₂SiO₄. *Appl Phys Lett* 85(2):209–211. <https://doi.org/10.1063/1.1769593>
- Watson EB, Chemiak DJ, Hanchar JM, Harrison TM, Wark DA (1997) The incorporation of Pb into zircon. *Chem Geol* 141(1):19–31. [https://doi.org/10.1016/S0009-2541\(97\)00054-5](https://doi.org/10.1016/S0009-2541(97)00054-5)
- Watson EB, Cherniak DJ (1997) Oxygen diffusion in zircon. *Earth Planet Sci Lett* 148(3):527–544. [https://doi.org/10.1016/S0012-821X\(97\)00057-5](https://doi.org/10.1016/S0012-821X(97)00057-5)
- Whitney DL, Evans BW (2010) Abbreviations for names of rock-forming minerals. *Am Miner* 95(1):185–187. <https://doi.org/10.2138/am.2010.3371>
- Wiedenbeck M (1995) An example of reverse discordance during ion microprobe zircon dating: an artifact of enhanced ion yields from a radiogenic labile Pb. *Chem Geol* 125(3):197–218. [https://doi.org/10.1016/0009-2541\(95\)00072-T](https://doi.org/10.1016/0009-2541(95)00072-T)
- Wiedenbeck M, Allé P, Corfu F, Griffin WL, Meier M, Oberli F, Quadt AV, Roddick JC, Spiegel W (1995) Three natural zircon standards for U-TH-PB, LU-HF, trace element and ree analyses. *Geostand Newslett* 19(1):1–23. <https://doi.org/10.1111/j.1751-908X.1995.tb00147.x>
- Zhang M, Salje EKH, Farnan I, Graeme-Barber A, Daniel P, Ewing RC, Clark AM, Leroux H (2000) Metamictization of zircon: Raman spectroscopic study. *J Phys Condens Matter* 12(8):1915–1925. <https://doi.org/10.1088/0953-8984/12/8/333>
- Zhang Y (2010) Diffusion in minerals and melts: theoretical background. *Rev Miner Geochem* 72(1):5–59. <https://doi.org/10.2138/rmg.2010.72.2>

Publisher's Note Springer Nature remains neutral with regard to jurisdictional claims in published maps and institutional affiliations.